Title
Ultra-high resolution fluorescence microscopy and its application in biology

Permalink
https://escholarship.org/uc/item/205177jr

Author
Shao, Lin

Publication Date
2005

Peer reviewed|Thesis/dissertation

Ultra-High Resolution Fluorescence Microscopy
and Its Application in Biology

by

Lin Shao

DISSERTATION

Submitted in partial satisfaction of the requirements for the degree of

DOCTOR OF PHILOSOPHY

in
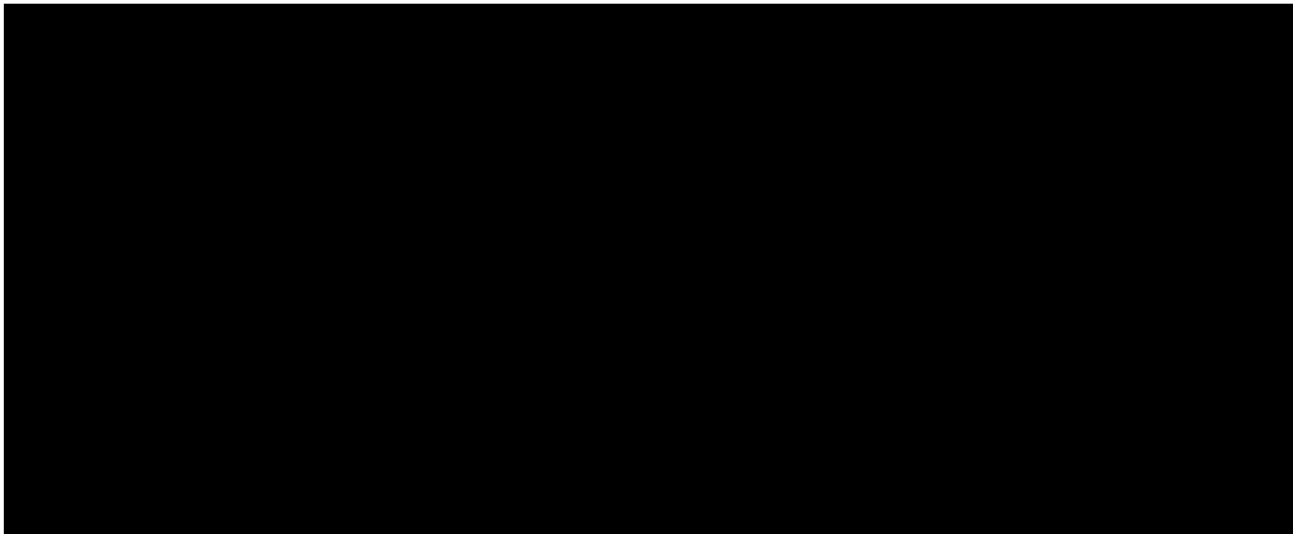
BIOLOGICAL AND MEDICAL INFORMATICS

in the

GRADUATE DIVISION

of the

UNIVERSITY OF CALIFORNIA, SAN FRANCISCO

Date   University Librarian

Degree Conferred:

Ultra-High Resolution Fluorescence Microscopy

and Its Application in Biology

Copyright ©2005

by

Lin Shao

To my parents.

Acknowledgments

It has been five intriguing years working in the Sedat Lab on my thesis project. I owe a great deal to Dr. Sedat for taking me as his student even though I didn't possessed much background relevant to the project I eventually took on. Dr. Sedat illustrated to me, not by words but by action, what it takes to become a good scientist — the willingness to think unconventionally, the perseverence at tackling hard problems, and the interdisciplinary approach to science and the ability to inspire people from different fields to jump in the bandwagon. John's best biology lesson to me: a fly is a human that flies.

I am also largely indebted to Dr. Mats Gustafsson, a former lab member who now has his own lab at UCSF. When he had to leave the lab in 2001, his unfinished project "conveniently" became my thesis project. He has been a trememdous help to me, both theoretically and experimentally, ever since the first day I joined the lab when I virtually knew nothing about microscope. I often feel spoiled by the presence of such a omnicient mentor. Through Mats, I learned that a true scientist needs to have a firm grasp of his core discipline from inside out, enjoys puzzle solving during experiment and not leaving any unexpected observation unexplained.

I'd also like to thank Dr. David Agard for coming to our group meeting almost always and giving insightful critiques to my project. The other thesis committee member, Dr. Tom Ferrin also gave valuable suggestions during thesis committee meetings. He has also provided lots of help in general as the Chair of our graduate program.

It's been great fun working toghether with previous and current lab members. I'm grateful to the cheerfulness of Brian Harmon, Michael Lowenstein, Bridget Hanser, Julio Vazquez, Felix Aburto, Satoru Uzawa, Emerick Gallego, Sara Abrahamsson, Sebastian Haase, Erik Hom, Yuri Strukov, Lukman Winoto, Heather McCune, Suchie Bhattacharyya, Goran Johansson, Shawn Zheng. Without those folks' company, the graudate school days can only be said good but not great.

I'm very grateful to my parents' patience and support even though I have been an ocean away from them. They are the most loving parents one can find anywhere. I'm also very fortunate to have Claire in my last year. She is a very entertaining company and always has a thought for other people. In hard times, she keeps her optimisim and support to me. Everytime I went to see my oncologist,

she would come with me.

Finally, I want to thank all the nurses, custodians, doctors for the world-class health care they provided me during my stay at 11th floor of the Long hospital.

Abstract

Ultra-High Resolution Fluorescence Microscopy

and Its Application in Biology

by

Lin Shao

Doctor of Philosophy in Biological and Medical Informatics

University of California, San Francisco

Professor John W. Sedat, Chair

Several new resolution enhancement schemes for fluorescence microscopy are experimentally implemented and tested using beads and biological samples. The first scheme, 3D structured illumination microscopy (SIM), makes use of the simple fact that fluorescence emission is the multiplication of the illumination and the sample's dye structure. If the illumination is structured such as a sinusoidal pattern, the recorded image would contain high-frequency components encoded in terms of low frequencies. In so doing, normally undetectable high-resolution information is given a chance to appear in the observable region, and is thus made *effectively* detectable. We are able to double the resolution both laterally and axially of the conventional microscope with 3D SIM. The second scheme, called I^5S, also uses structured illumination, but with a Sagnac-like interferometer setup consisting of two opposing objective lenses used for illumination and fluorescence detection. Interference in both illumination, which gives rise to more complicated structured illumination pattern than 3D SIM, and detection can be achieved. The combined interferometric effect is seven-fold enhancement in axial resolution as well as doubled lateral resolution. Finally, we introduce a more complicated I^5S scheme in which both emission wavefronts, instead of just one of them, are recorded by two CCD cameras simultaneously. The complementary phase relationship between the two wavefronts can be utilized in estimating and then correcting the phase error often difficult to avoid in I^5S experiments.
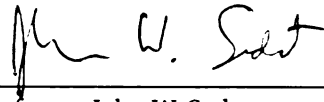
Professor John W. Sedat
Dissertation Committee Chair

Table of Contents

List of Figures

Chapter 1

Introduction

1.1   Resolution limit in three-dimensional wide-field optical microscopy

The optical microscope (OM) is an invaluable tool for biology. Among all the different imaging modalities, OM is favored by biologists due to its low sample damage, high specificity due to fluorescence labeling, and the ease with which it produces three-dimensional (3D) structures of the interior of cells. On the other hand, OM's major drawback is its relatively low spatial resolution. In order to better present resolution enhancement technologies, the main theme of this thesis, it is necessary to prepare the reader with the basics of the resolution limit.

The problem addressed throughout this thesis is imaging under incoherent illumination. Under this condition, it is well known that the imaging system is linear shift invariant (LSI) [5, Sec. 9.5]. That is, it acts like a linear filter in frequency space or a convolutor in real space. In 3D spatial frequency space, the object $\widetilde{F}$ and its image $\widetilde{G}$, both expressed as a superposition of harmonic components of all possible frequencies $\vec{k}$, are related via

$$\widetilde{G}(\vec{k}) = \widetilde{F}(\vec{k})O(\vec{k})^1.$$ (1.1)

From this formula, it is clear that the imaging properties of an OM are completely encapsulated in

---

[1]Noise contamination in the image is ignored for the moment.

(a) k_z $NA = n\sin\alpha$ (b) k_z

$r = 2\pi n/\lambda$

α r k_y

k_y

$r(1-\cos\alpha)$

$2r\sin\alpha$
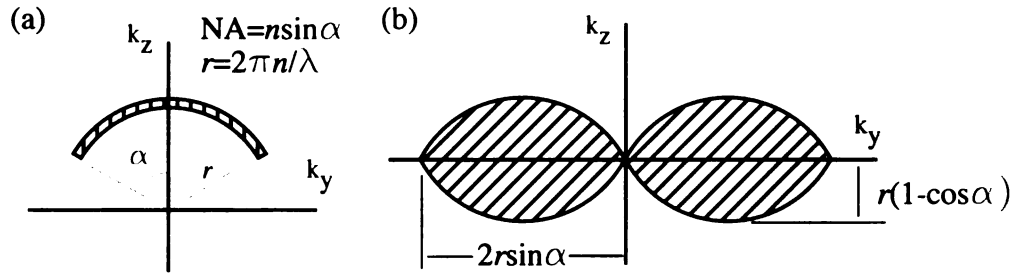
Figure 1.1: (a) The generalized pupil function, OTF_A, of an objective lens only has nonzero values on a finite 2D surface of a spherical cap. The shape of this cap is governed by the acceptance angle α of the lens, the wavelength of the light, and the refractive index of the immersion medium. (b) The OTF of the lens is the auto-correlation of OTF_A, which gives rise to a finite region of nonzero values, called the OTF support or observable region of the objective lens (the hatched region). (NA: numerical aperture)

$O(\vec{k})$, the frequency response function or optical transfer function (OTF) of the imaging system. It is shown [5, Sec. 9.5] that the OTF is the auto-correlation of the generalized pupil function of the system (denoted by OTF_A). OTF_A is a two-dimensional surface on a spherical cap in the frequency space [18] as shown in Fig. 1.1a. OTF_A is nonzero only within a certain boundary determined by the objective lens' acceptance angle (α in Fig. 1.1a). Because of the finite extent of OTF_A, the OTF also has a finite region where its value is nonzero (Fig. 1.1b) as a result of the auto-correlation. This region is called the microscope's OTF *support*, also known as the *observable region* since the object's harmonic components of only those frequencies within this region can be detected by the microscope. All higher-frequency information outside of the OTF support are lost due to the linear filtering effect. Therefore, the boundary of the OTF support defines the resolution limit of the microscope.

In real space, the LSI imaging model implies that the descriptor of the resolution limit is the intensity point spread function (PSF), the image of an ideal point source (Airy rings), as an image is formed by a convolution of the PSF P and the object F,

$$G(\vec{r}) = P(\vec{r}) \otimes F(\vec{r}), \tag{1.2}$$

which is the frequency-space counterpart of (1.1). The fact that the PSF is a "blurred" version of the point source results in the minimal distance between two point sources, below which the image of them appears as a single point (Fig. 1.2).
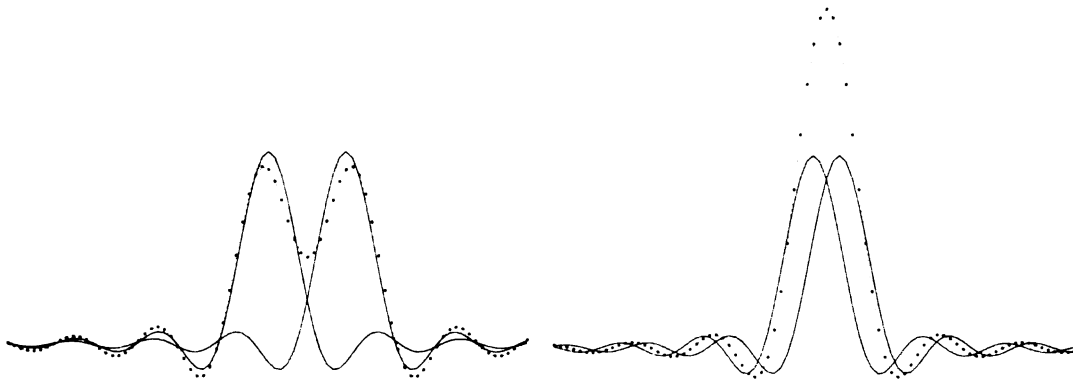
Figure 1.2: Point spread function and the resolution limit. On the left, when the two point sources are spaced sufficiently apart, the resultant image (the dotted curve), which is the sum of the two individual images of the sources (the solid curves) still shows two resolvable points. On the right, however, when the two points are too close, the image appears as if only one point source is present.

1.2 Outline

The rest of the thesis is divided into three chapters. In Ch. 2, we will discuss the resolution enhancement principle and experimental results of structured illumination microscopy (SIM). In brief, SIM makes use of a simple fact in fluorescence OM — the fluorescence emission is the multiplication of the illumination and the sample's dye structure. If the illumination is structured as a sinusoidal pattern, the recorded image would contain high-frequency components encoded in terms of low frequencies. In so doing, normally undetectable high-resolution information is given a chance to appear in the observable region, and is thus made *effectively* detectable. In our prototype SIM, we accomplished doubled resolution in both lateral and axial directions compared to conventional OM. Comparison between images taken with conventional and SIM will be presented to demonstrate the benefit of enhanced resolution.

In Ch. 3, a different but related scheme called I^5S will be introduced.[2] Structured illumination again is used, but the main feature of I^5S is its Sagnac-like interferometer consisting of two opposing objective lenses used for illumination and fluorescence detection. Interference in both illumination and detection can be achieved. The combined interferometric effect is a seven-fold enhancement in axial resolution as well as doubled lateral resolution. Experimental results will be shown to

---

[2]I^5S stands for Imaging Interference and Incoherent Illumination Interference plus Structured illumination

demonstrate the drastically enhanced resolution of I^5S.

I^5S uses a beam splitter to combine the two wavefronts detected by the two objective lenses. It is normally sufficient to detect only the emission wavefront from one of the two exits of the beam splitter. However, in Ch. 4, we will see that it is also useful to detect the wavefront coming out of the second exit because the two wavefronts have complementary phases. This relationship can be utilized in estimating and then correcting the phase error that is often difficult to avoid in I^5S experiments. Proof-of-principle experiments with fluorescent beads were conducted and the results will be shown.

Chapter 2

Structured Illumination

The fluorescence microscope, a type of OM, is an indispensable tool for biology mainly because it is capable of selectively imaging molecules of interest in the sample. However, like all OMs, it is subject to the resolution limit imposed by the physical law of diffraction. A 3D wide-field fluorescence microscope's resolution capability can be described in frequency space by the so-called observable region (Fig. 2.1(a)). Only for frequencies from within this region can the microscope detect the harmonic components of the sample (or more precisely, the fluorescence signal emitted from the sample's dye). The shape of the observable region implies one particular shortcoming of OM — very poor axial resolution, especially for low-resolution components surrounding the origin of the frequency space (the missing cone in Fig. 2.1(a)). In other words, there is little sectioning (or depth-discrimination) capability if 3D imaging is needed because out-of-focus signals from surrounding planes can severely contaminate the image of the focal section. To alleviate this problem, constrained iterative deconvolution has been introduced [1] to computationally remove the out-of-focus signal so as to achieve sectioning effect. Even though the missing cone is somehow filled in by applying *a priori* constraint in this method, it can be argued that it never recovers the physically lost information. The confocal laser scanning microscopy [28] is the first technology with true optical sectioning capability, achieved by physically rejecting the out-of-focus light through a pair of pinholes. The major drawback of confocal microscopy is its low light efficiency, as most of the emission light is discarded by the pinhole. Practical biological samples are often too weakly fluorescent to af-

ford losing signal this way. Optical sectioning can also be achieved based on the simple principle that only illuminated parts of the sample emit fluorescence. In two-photon microscopy [8], simultaneous absorption of two photons by fluorescent molecules results in an axially confined illumination region and thus depth discrimination. In terms of light efficiency, it is better than confocal microscopy since a single IR photon cannot excite the fluorophores below and above the focal plane. Selective plane illumination microscopy (SPIM) [22] realizes a confined illumination plane by forming a sheet of laser light that illuminates a thin layer of the sample, thus achieving optical sectioning. It is best suited for very thick tissue samples.

Optical sectioning greatly improves the utility of OM in 3D imaging, but it is still subject to the diffraction limit. In theory, confocal microscopy can detect extended-resolution information weakly [14], but only if operated with a pinhole that is significantly smaller than the Airy disc [38], by which even more light would be discarded. Therefore the practical merit of such a scheme is minimal. One feasible resolution-extension scheme based on confocal microscopy is STED (stimulated emission depletion) [25]. In STED, a very short (compared to the fluorescence lifetime) pulse is applied so as to deplete the fluorophores in the excited state. If the STED pulse is engineered so that it only quenches the fluorophores surrounding the excitation peak, the emission point spread function (PSF) is then shrunk.

In my project, we want to ask whether one can build on top of wide-field microscopes a system that can both break the physical resolution limit and have optical sectioning capability. Part of the answer to this question already lies in the principle behind two-photon, SPIM, and STED — only the fluorescent molecules that actually emit light can be detected. Mathematically, this means

$$E(\vec{r}) = I(\vec{r})D(\vec{r}), \tag{2.1}$$

namely the emission light distribution equals to the multiplication of the illumination and the dye density. If the excitation pattern is spatially varying, such as those in references [11, 15, 19], high-resolution information can be encoded into the observed emission light in a manner very similar to the Moiré fringe phenomenon. The basic concept is explained in Fig. 2.1. A sinusoidal excitation pattern (Fig. 2.1(b)) is projected onto the sample. In the frequency space, this pattern corresponds to the sum of three Delta functions shown in Fig. 2.1(c). Following the convolution theorem, it

can be shown that the Fourier transform of the observed emission light is the sum of the sample's spectrum and the two displaced versions of it (Fig. 2.1(d)). Some high-frequency components in the sample's spectrum normally outside of the observable region are thus "pulled" into that region and become effectively observable (Fig. 2.1(e)). In other words, the effective OTF support is enlarged and therefore resolution extended beyond the diffraction limit. Of course, post-processing is required to handle the extraction and reconstruction of the high-frequency components.

On the other hand, people have also used standing-wave illumination to enhance axial resolution [2, 12, 16, 29]. In [29], a lateral grid pattern is projected onto the sample such that an optically sectioned image is obtained by extracting only those parts of the image where the grid pattern is visible and then mathematically removing the grid pattern. In the other cases [2, 12, 16], an interferometer consisting of two opposing objective lenses are used to generate an axial illumination pattern. Together with detection interference, axial resolution can thus be greatly enhanced. In Ch. 3 a scheme combining the interferometer and structured illumination will be presented in detail. For the moment, the reader just needs to bear in mind that this scheme can achieve better than 100nm axial resolution, although at the cost of a rather complicated interferometer setup as well as stringent requirements for sample preparation.

In this chapter, we will discuss the principle 3D SIM which can double both lateral and axial resolution and achieve physical optical sectioning. This project is an extension to the 2D SIM reported in [15]. Throughout the discussion, the following notations will be used. $\vec{r}$ and $\vec{k}$ are real- and frequency-space coordinates respectively, $\vec{r}_t = (x, y)$ is the lateral component of $\vec{r}$, $\vec{k}_t = (k_x, k_y)$ is the lateral component of $\vec{k}$, $P(\vec{r})$ is the PSF, and $O(\vec{k})$ is the OTF.

2.1 Concepts

As in 2D SIM [15], 3D SIM's theoretical basis lies in the fact that the object of interest to the microscopist is not actually the emission light $E(\vec{r})$ but rather the sample structure: the density distribution of fluorescent dye $D(\vec{r})$. They are related by Eq. 2.1. The Fourier transform of this point-wise product is a convolution: $\widetilde{E}(\vec{k}) = (\widetilde{I} \otimes \widetilde{D})(\vec{k})$. The convolution operation is non-local, and
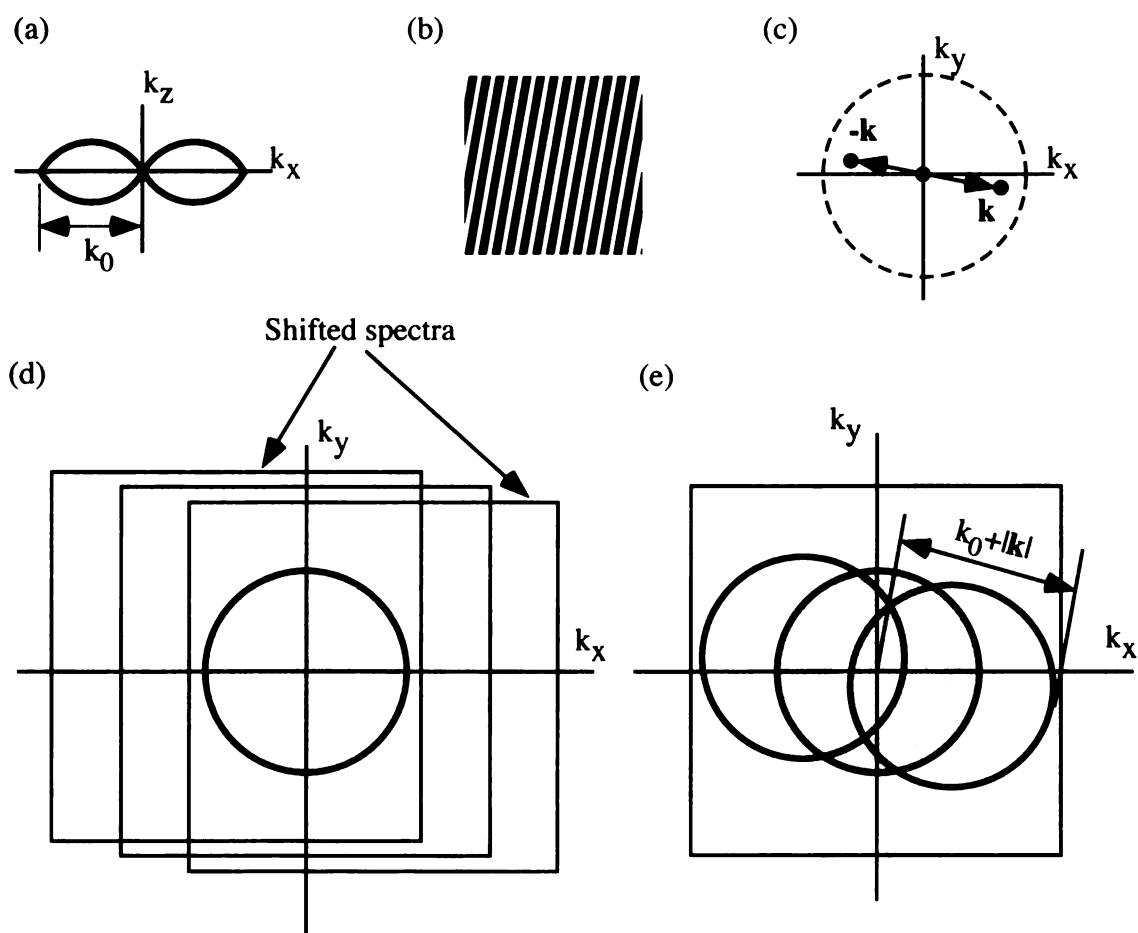
Figure 2.1: The concepts of lateral resolution extension using 2D structured illumination. (a) shows the intersection of the 3D OTF support by any plane in which k_z axis lies. A lateral illumination pattern in (b) corresponds to the sum of three Delta functions represented by the 3 dots in the frequency space in (c), where the dashed circle is the lateral boundary of the OTF support. Using this patterned illumination, the observed emission signal, in frequency space, is the sum of the sample's spectrum and the two displaced versions of it, all represented as a square in (d). The displaced spectra are shifted from the origin by $\pm\vec{k}$ shown in (c). As a result, the frequencies within the two circles shifted by $\pm\vec{k}$ from the origin, as shown in (e), of the sample's spectrum become effectively observable. The unshaded regions in the two shifted circles represent the high-resolution information undetectable to a conventional microscope.

in particular can make the observed data within the observable region of $\widetilde{E}(\vec{k})$ depend on normally unobservable components of $\widetilde{D}(\vec{k})$ from other parts of the frequency space. That information is then observable in principle, but must be extracted.

To extract that information is nontrivial for general illumination patterns, but becomes simple if a few conditions are satisfied. First, the illumination pattern should be a sum of a finite number of components, each of which is separable into an axial and a lateral function:

$$I(\vec{r}_t, z) = \sum_m A_m(z) L_m(\vec{r}_t) \tag{2.2}$$

Second, when the 3D data are acquired as a sequence of 2D images with different focus, the illumination pattern should be maintained fixed in relation to the focal plane of the microscope, not in relation to the sample. In that case, the axial part of each illumination component multiplies the PSF, not the sample, in the convolution integral:

$$\begin{aligned} G_m(\vec{r}_t, z) &= \iint D(\vec{r}_t - \vec{u}, z - v) L_m(\vec{r}_t - \vec{u}) A_m(v) P(\vec{u}, v) \, \mathrm{d}\vec{u}\mathrm{d}v \\ &= (A_m P)(\vec{r}) \otimes (L_m D)(\vec{r}) \\ \Rightarrow \widetilde{G}_m(\vec{k}) &= O_m(\vec{k}) \left(\widetilde{D}(\vec{k}) \otimes \widetilde{L}_m(\vec{k}) \right), \end{aligned} \tag{2.3}$$

where $O_m(\vec{k}) = (\widetilde{A}_m \otimes O)(\vec{k})$ is the Fourier transform of $(A_m P)(\vec{r})$.

If finally each L_m is a simple harmonic,

$$L_m(\vec{r}_t) = 2\cos(\vec{k}_{0,m} \cdot \vec{r}_t + \phi_m), \tag{2.4}$$

so that

$$\widetilde{L}_m(\vec{k}_t) = e^{-i\phi_m} \delta(\vec{k}_t - \vec{k}_{0,m}) + e^{i\phi_m} \delta(\vec{k}_t + \vec{k}_{0,m}),$$

then the observed data has the form

$$\widetilde{G}(\vec{k}) = \sum_m O_m(\vec{k}) \left(e^{-i\phi_m} \widetilde{D}(\vec{k} - \vec{k}_{0,m}) + e^{i\phi_m} \widetilde{D}(\vec{k} + \vec{k}_{0,m}) \right), \tag{2.5}$$

a sum of a finite number of copies of the sample information $\widetilde{D}(\vec{k})$, each moved laterally in frequency space by a distance $\pm\vec{k}_{0,m}$, multiplied by a transfer function $O_m(\vec{k})$, and phase shifted by $\pm\phi_m$. These components must still be separated. This can be done by acquiring additional data sets with different known phases ϕ_m, thus generating linearly independent combinations of the components. If there

are N independent components, these can be separated by a simple matrix inversion after acquiring data with at least N different phases.

The data contain new information in two ways: the support of each transfer function O_m is extended axially compared to the conventional OTF O, through the convolution with the axial function $\tilde{A}_m$, and the translation by $\pm \vec{k}_{0,m}$ moves new information into the (laterally unchanged) support of O_m. As O_m and $\vec{k}_{0,m}$ are known, the different components can be computationally moved back to their true positions in frequency space, recombined into a single extended-resolution data set, inverse filtered, and inverse Fourier transformed to real space (see Sec. 2.2.3).

The observable region with this method becomes the support of the convolution of the conventional OTF with the illumination structure. Since the set of Fourier components that can be generated in the illumination is limited by diffraction in exactly the same way as the set of components that can be observed (scaled by the ratio of emission and excitation wavelengths), the maximum resolution extension possible in this manner (if the illumination and observation takes place through the same optical system) is about a factor of two in each dimension.

In the 2D SIM used previously [15], the sample was illuminated by two beams of light, which interfered to form a sinusoidal light intensity pattern $1 + \cos(\vec{k}_0 \cdot \vec{r}_t)$, which has only three Fourier components (the black dots on k_r axis in Fig. 2.2b). If the same illumination pattern were applied in 3D, the resulting observable region would consist of three shifted copies of the conventional OTF (the closed regions bisected by k_r axis in Fig. 2.2e). That region yields twice the normal lateral resolution, but suffers from the same missing cone problem as the conventional OTF, making 3D reconstructions difficult. One way around this problem would be to use a coarser illumination pattern, which would move the 3 OTF components closer together, allowing them to overlap each other's missing cones. However, that approach, which is used in [29], sacrifices lateral resolution. That trade-off can be avoided by using a more complex illumination structure. In the 3D SIM used in this thesis, the fluorescent sample is illuminated with 3 mutually coherent beams of excitation light (Fig. 2.2a). The resulting 3D excitation intensity pattern contains 7 Fourier components, corresponding to all possible difference vectors between the three illumination wave vectors (Fig. 2.2b), resulting in the observable region in Fig. 2.2(e, f). This region fills in the missing cones while

(a)

(b)

(c)

(d)

(e)

(f)

(g)
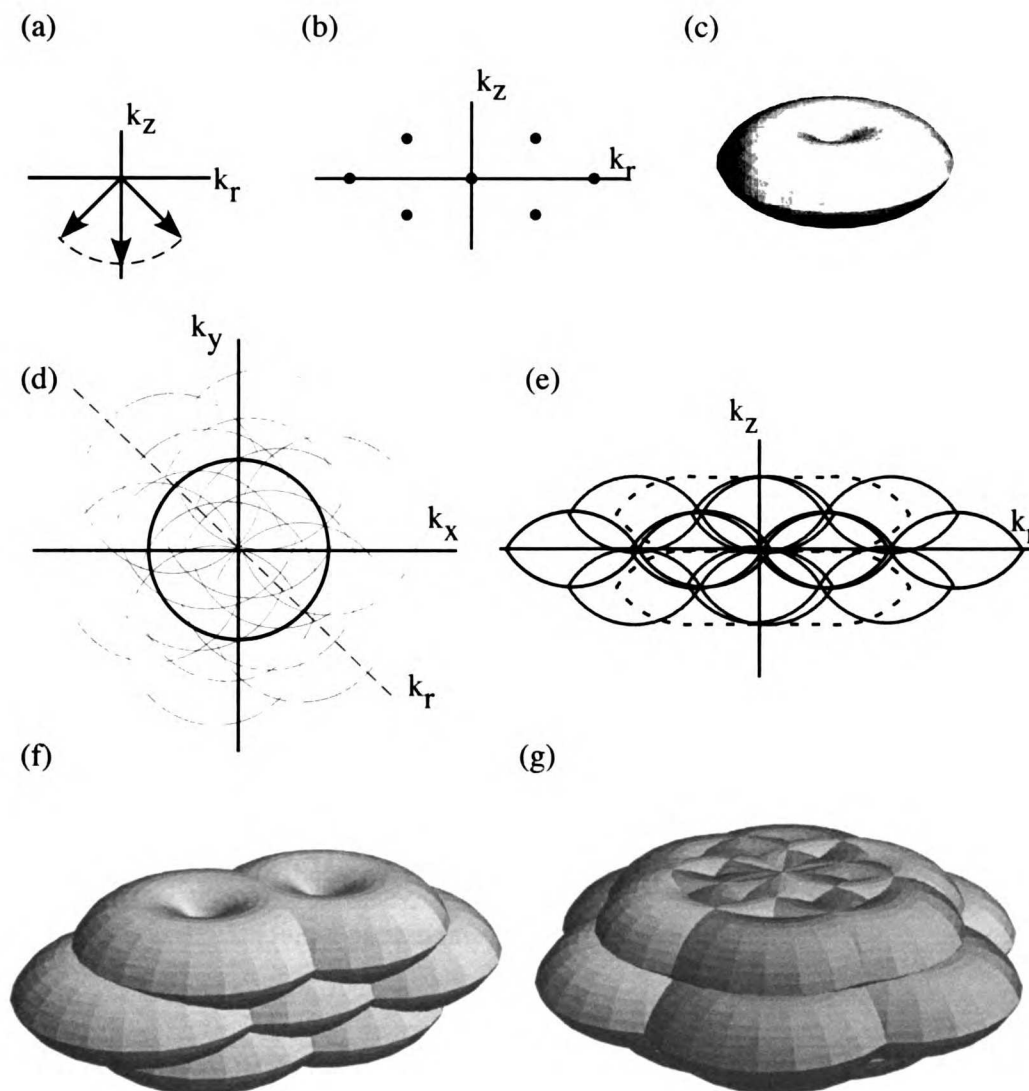
Figure 2.2: The concepts of 3D structured illumination. Three temporally coherent illumination wavefronts, represented as three arrows in frequency space in (a), interfere with each other to generate lateral and axial sinusoidal patterns, shown in (b) as δ functions located on a k_z–k_r plane of the frequency space (the same plane as in (a)). Under such illumination, parts of the sample spectrum along the k_r direction, which are outside the normal observable region (the thick circle in (d)), become effectively observable as explained in the text and Fig. 2.1. After applying the illumination pattern at two additional angles, the lateral resolution extension becomes approximately isotropic (d). The effective observable region can be thought of as the convolution of the illumination structure and the normal observable region (see text), which results in the axial resolution enhancement shown in (e). The regions enclosed in dashed lines are made effectively observable by applying other orientations of the illumination patterns. (c), (f), and (g) are 3D rendering of the observable region when there is no structured illumination, there is structured illumination with one lateral pattern orientation, and with all three lateral orientations respectively.

maintaining the full factor of two of lateral resolution extension, and at the same time doubles the axial resolution. It extends lateral resolution only in one direction, but the procedure can of course be repeated with the illumination pattern rotated to other directions. Fig. 2.2d shows the almost isotropically enlarged lateral observable region using three pattern orientations, and 3D rendering of the effective observable region under such condition is shown in Fig. 2.2g.

In our implementation of 3D SIM, the three illumination beams were generated from a slightly spatially incoherent beam using a diffraction grating. The resulting illumination can be thought of as an incoherent sum of the interference of many beam triplets as in Fig. 2.2b, with different overall direction but with the same relative lateral wave vector differences within each triplet. This makes the side spots in Fig. 2.2(b) take on a finite extent axially but not laterally. The illumination structure thus remains of the form required by Eqs. 2.2 and 2.4. The incoherence simply causes a slight axial broadening of the OTF side bands (see Sec. 2.3) in Fig. 2.2(e–g). Some incoherence helps suppress stray interference fringes from dust particles etc, which could otherwise cause artifacts. As the laser beam's spatial coherence is lost, so is its original polarized state. However, S-polarization of the beams is preferable for generating illumination fringes with high modulation depth and thus strong signal from outside of the normal observable region. We therefore re-polarized the beam and maintain the S-polarization for all pattern orientations (see Sec. 2.2.1).

2.2 Implementation

2.2.1 Optomechanical setup

A prototype 3D SIM has been constructed (Fig. 2.3). Laser light was spatially scrambled by a rotating holographic diffuser (Physical Optics Corp., Torrance, CA) to remove spatial coherence, and coupled into a multi-mode optical fiber (core size 100 μm, numerical aperture 0.12, Cer-amoptec, (East Longmeadow, MA). The light exiting the fiber was collimated, linearly polarized, and directed to a linear transmission phase grating (custom made by Diffraction Limited, Canada), which diffracted the beam into a large number of orders. A beam block discarded all orders except orders -1, 0 and +1. The grating was designed so that the intensity of order 0 was about 80% of

that of orders 1 and it diffracts 75% of the incoming light power into these three orders. The three remaining orders were refocused so that each formed an image of the fiber end face in the back focal plane of the objective lens. Orders +1 and -1 were focused near opposing edges of the back focal plane aperture, and order 0 at its center. The objective lens (Nikon PlanApo 100X 1.4 NA, 160 mm conjugate) re-collimated the beams and made them intersect each other in the objective focal plane, where they interfered to form an illumination intensity pattern that can equivalently be thought of as a demagnified image of the grating. Fluorescence light emitted by the sample was deflected by a dichroic mirror to a cooled CCD camera; scattered excitation light was rejected by an emission filter in front of the camera. A 3D dataset is acquired by translating the sample stage axially relative to the objective lens using a piezoelectric actuator (Queensgate Instruments, Torquay, UK) close-loop controlled using a capacitive distance sensor (Queensgate Instruments). The orientation and phase of the illumination pattern were controlled by rotating and laterally translating the grating. For this purpose, the grating was mounted on a piezoelectric translator (Piezosystem Jena, Jena, Germany), which in turn was mounted on a motorized rotation stage (National Aperture, Salem, NH). The piezoelectric translator was controlled in closed loop using a custom-made capacitive distance sensor, which consisted of one convex electrode that was part of the grating holder, and one hollow cylindrical counter-electrode that surrounded the grating holder. The counter-electrode, which was rigidly attached to the optical table, served as a fixed reference, so that the position of the grating could be controlled with nanometer precision and reproducibility without placing any unusual requirements on the rotation stage. S-polarization of the beams was maintained at all orientations by a linear polarizer that co-rotated with the grating.

2.2.2 Image acquisition

Focal series of images are acquired in SIM by translating the sample stage axially via sending computer commands to a closed-loop controlled piezoelectric nano-positioning system. The raw

CCD

Σ1

linear
polarizer

dichroic mirror

L3

L2

L1

phase grating

L0

sample
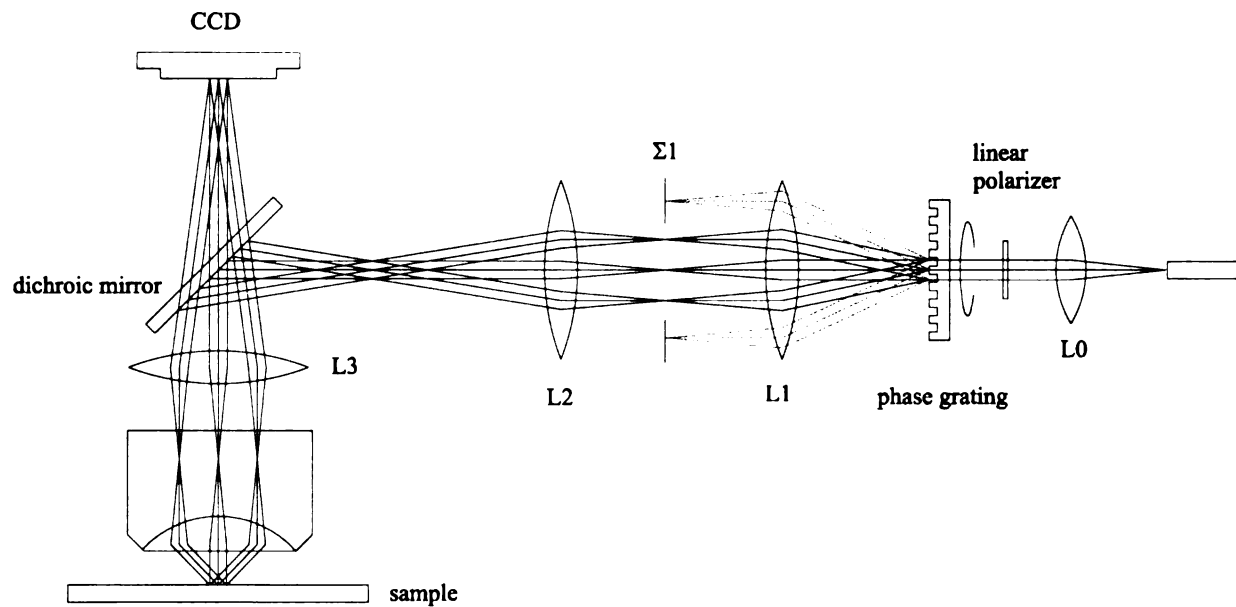
Figure 2.3: The 3D structured illumination microscope. Illumination light is relayed into the system through a multimode optic fiber, collimated by lens L0, S polarized, and diffracted by a phase grating placed at a secondary image plane. From the multitude of diffraction orders, orders 0, +1, and -1 are allowed to pass on and illumination at the sample as three plane waves, which then interfere to form both lateral and axial sinusoidal patterns. (Plane Σ1 is conjugate to the objective lens' back focal plane.) The phase grating, together with the polarizer, can be rotated around the optic axis so that any orientation of the lateral pattern can be generated. The phase grating is also transversely driven by an piezoelectric actuator so as to change the phase of the lateral pattern, which is necessary for raw data separation.

data contains five components added together:

$$\widetilde{G}(\vec{k}) = 2O(\vec{k})\widetilde{D}(\vec{k}) \quad + \quad O_1(\vec{k})\left(e^{-i\phi}\widetilde{D}(\vec{k}-\vec{k}_0/2) + e^{i\phi}\widetilde{D}(\vec{k}+\vec{k}_0/2)\right)$$
$$+ \quad O_2(\vec{k})\left(e^{-i2\phi}\widetilde{D}(\vec{k}-\vec{k}_0) + e^{i2\phi}\widetilde{D}(\vec{k}+\vec{k}_0)\right), \qquad (2.6)$$

which is a special form of Eq. 2.5. In order to extract the five terms from the sum (2.6), we need to take five images with five different values of ϕ and solve a system of five linear equations, the same approach used in 2D SIM [15]. ϕ can be altered as discussed in the previous subsection. At each focal position, five images are taken with five preset phase positions of the grating stage. After a focal series is taken under the illumination of one lateral pattern orientation, the same process is repeated for two other orientations 60° and 120° apart from the first one by sending computer commands to the motor that controls the rotational stage. In the end, a dataset thus acquired is organized as three separate stacks, each corresponding to one grating (or pattern) orientation. Each stack is a focal series of images taken at 122 nm focus intervals. Furthermore, at every focal position, five images are acquired with different grating phase settings.

2.2.3 Image reconstruction

Preprocessing

Table 2.1: The "bands" representation of Eq. 2.6 terms

(2.6) terms	Denoted as
$O(\vec{k})\widetilde{D}(\vec{k})$	$\widetilde{B}_0$
$O_1(\vec{k})e^{-i\phi}\widetilde{D}(\vec{k}-\vec{k}_0/2)$	$\widetilde{B}_{1+}$
$O_1(\vec{k})e^{i\phi}\widetilde{D}(\vec{k}+\vec{k}_0/2)$	$\widetilde{B}_{1-}$
$O_2(\vec{k})e^{-i2\phi}\widetilde{D}(\vec{k}-\vec{k}_0)$	$\widetilde{B}_{2+}$
$O_2(\vec{k})e^{i2\phi}\widetilde{D}(\vec{k}+\vec{k}_0)$	$\widetilde{B}_{2-}$

Several steps precede the real image reconstruction. After CCD dark image subtraction and flat-fielding [21], the first step is a simple 5 × 5 matrix inversion, after which the inverted matrix is applied to each of the three raw data stacks to separate the five components of Eq. 2.6 (notations listed in Table 2.1 will be used hereinafter for these components). The details of the separation

step can be found in Appendix A. Since the $\widetilde{B}_0$ components from each stack are supposed to be identical, they are used as the reference to, for each focal section, equalize the intensity between the first and the other two stacks. $\widetilde{B}_0$ components are also used for estimating the displacement of the second and third stacks relative to the first, simply by cross-correlating between the first and the other two stacks' $\widetilde{B}_0$ components. This displacement correction is necessary because thermal or mechanical drift can cause significant displacements during data acquisition, which usually requires 5–20 minutes depending on sample thickness.

The next step accomplishes two things at the same time: fine-tuning the vector $\vec{k}_0$ and the estimation of the complex modulation amplitudes that relates $\widetilde{B}_0$ with $\widetilde{B}_{1+}$, $\widetilde{B}_{1-}$, $\widetilde{B}_{2+}$, and $\widetilde{B}_{2-}$. For example, in theory $M_{2+} = 1.0$ in the following relationship between $\widetilde{B}_0$ and $\widetilde{B}_{2+}$:

$$M_{2+} \cdot O_2(\vec{k} - \vec{k}_0)\widetilde{B}_0(\vec{k}) = O(\vec{k})\widetilde{B}_{2+}(\vec{k} - \vec{k}_0). \tag{2.7}$$

For this to be exactly true, however, the illumination's modulation depth must be exactly the same as when the OTF data was acquired, and its phase ϕ_m must be zero. This is not generally the case in reality because the illumination's modulation depth can vary depending on imaging conditions, and ϕ_m in Eq. 2.4 is arbitrary without a reference point, ϕ_0 , which is generally different for each dataset[1]. Therefore in reality, M_{2+} is not 1.0, but a complex number Ae^{ϕ_0} instead. Likewise between $\widetilde{B}_0$ and all other components listed in Table 2.1 of each pattern orientation, there exists a complex amplitude that needs to be estimated (except that it can be shown that M_{m+} equals the complex conjugate of M_{m-}). Also to be estimated is $\vec{k}_0$, which, although known through calibration, can be slightly altered due to mechanical instability from experiment to experiment. Our scheme for jointly estimating the modulation amplitudes and $\vec{k}_0$ are, using $\widetilde{B}_{2+}$ for demonstration, as follows:

1. Use the current estimates of $\vec{k}_0$ to carve out the region from $\widetilde{B}_0$ overlapping with $\widetilde{B}_{2+}$ and multiply it by $O_2(\vec{k} - \vec{k}_0)$ (denoted as $\widetilde{B}_0^{2+}$), and the region from $\widetilde{B}_{2+}$ overlapping with $\widetilde{B}_0$ and multiply by $O_0(\vec{k} + \vec{k}_0)$ (denoted as $\widetilde{B}_{2+}^0$).

2. Translate $\widetilde{B}_{2+}^0$ by $\vec{k}_0$ via multiplying $e^{j\vec{k}_0 \cdot \vec{r}}$ to $B_{2+}(\vec{r})$ in real space.

3. Obtain the current estimate of M_{2+} through a complex linear regression between all point

---

[1] ϕ_0 can be thought of as the lateral fringes' phase relative to the corner of a lateral section.

pairs $(B_{2+}^0(\vec{r}), B_0^{2+}(\vec{r}))$ for all points $\vec{r}$ in the overlap region.

4. Slightly modify the magnitude and/or angle of $\vec{k}_0$.

5. Repeat 2 to 4 until the amplitude (A) of the current estimate of M_{2+} does not increase significantly.

One half of the final estimate of $\vec{k}_0$ is then used for estimating the complex factor between $\tilde{B}_0$ and $\tilde{B}_{1+}$. The scheme is applied independently for all three pattern orientations.

Reconstruction — Linear inverse filtering

The maximum a posteriori (MAP) method with Gaussian noise model has proven to be effective and efficient for 3D microscopy image deconvolution [13, 37]. First, for the convenience of gradient operation later on, we introduce the vector form of the convolution equation (1.2): $\mathbf{g} = \mathsf{P}\mathbf{f}$. Here an object and its image are represented as vectors $\mathbf{f}$ and $\mathbf{g}$ respectively, and convolution is expressed as matrix P multiplying $\mathbf{f}$, where P is constructed from the PSF P [4, Sec. 2.2]. Under MAP framework with Gaussian noise model, image deconvolution is formulated as minimizing an objective function [37]: $\Phi(\mathbf{f}) = \|\mathsf{P}\mathbf{f} - \mathbf{g}\|^2 + \mu\|\mathsf{C}\mathbf{f}\|^2$, in which C is a filtering operator and μ is a positive regularization parameter. The first term (fidelity term) describes how well the guess $\mathbf{f}$ accounts for the raw image data $\mathbf{g}$. The second term is a penalty term that punishes noise amplification outside the band limit, and μ determines how much impact the penalty would have over the guess. SIM image reconstruction is in part a deconvolution problem, but more importantly a reassembly of all the information components into a single image with extended resolution. Therefore the MAP scheme needs modification to suit our purpose.

The preprocessing produces 15 raw data components, each of which in frequency space is of the form $\tilde{B}_i(\vec{k}) = O_i(\vec{k})\tilde{D}(\vec{k} - \vec{k}_{0i})$ (assuming that the complex modulation amplitude M_i has been divided out from each component). In real space, we can write them as $B_i(\vec{r}) = P_i(\vec{r}) \otimes [D(\vec{r})e^{-j\vec{k}_{0i}\cdot\vec{r}}]$, where $P_i(\vec{r})$ is the inverse Fourier transform of $O_i(\vec{k})$. Thus the objective function to minimize in SIM is a summation of terms:

$$\Phi(\mathbf{d}) = \sum \|\mathsf{P}_i\mathbf{d}_i - \mathbf{b}_i\|^2 + \mu\|\mathsf{C}\mathbf{d}\|^2, \tag{2.8}$$

in which P_i is built from $P_i(\vec{r})$ and d_i is the vector form of $D(\vec{r})e^{-j\vec{k}_{0i}\cdot\vec{r}}$. Eq. 2.8 can be shown to equal to

$$\Phi(\mathbf{d}) = \sum \left\| \widehat{P}_i\mathbf{d} - \widehat{\mathbf{b}}_i \right\|^2 + \mu \left\| C\mathbf{d} \right\|^2, \tag{2.9}$$

where $\widehat{P}_i$ is the matrix form of $P_i(\vec{r})e^{j\vec{k}_{0i}\cdot\vec{r}}$ and $\widehat{\mathbf{b}}_i$ is the vector form of $B_i(\vec{r})e^{j\vec{k}_{0i}\cdot\vec{r}}$. The gradient of $\Phi(\mathbf{d})$ is then (ignoring a scaling factor) $\nabla\Phi(\mathbf{d}) = \sum \left(\widehat{P}_i^t\widehat{P}_i\mathbf{d} - \widehat{P}_i^t\widehat{\mathbf{b}}_i \right) + \mu C^t C\mathbf{d}$, which, when set to zero, gives rise to the solution to $\mathbf{d}$:

$$\mathbf{d} = \left(\sum \widehat{P}_i^t\widehat{P}_i + \mu C^t C \right)^{-1} \sum \widehat{P}_i^t\widehat{\mathbf{b}}_i.$$

In Fourier space, the solution is in the format of an inverse filter:

$$\widetilde{D}(\vec{k}) = \frac{\sum O_i^*(\vec{k} + \vec{k}_{0i})\widetilde{B}_i(\vec{k} + \vec{k}_{0i})}{\sum |O_i(\vec{k} + \vec{k}_{0i})|^2 + \mu|\widetilde{C}(\vec{k})|^2}. \tag{2.10}$$

We note that linear inverse filtering is made possible by the shape of the SIM's OTF support (Fig. 2.2) which has no gaps. We let $\widetilde{C}(\vec{k})$ be constant everywhere in Fourier space and in essence implement a Wiener filter. The choice of μ depends on the signal-to-noise ratio (SNR) of the raw image — the higher the SNR the smaller μ. Practically in calculating the numerator of Eq. 2.10, $O_i^*(\vec{k})\widetilde{B}_i(\vec{k})$ is calculated first, then Fourier transformed to real space, and multiplied by a plane wave $\exp(j\vec{r}\cdot\vec{k}_{0i})$ so as to achieve sub-pixel accuracy in shifting by $\vec{k}_{0i}$ in frequency space, since $\vec{k}_{0i}$ usually is not a multiple of $\Delta\vec{k}$, the pixel size (μm^{-1}) in frequency space. Before inverse Fourier transforming back to real space, apodization [27, 30] is applied in order to minimize the ringing effect in the real space images that would otherwise result from the hard edge of the enlarged observable region. The entire image reconstruction takes about 2.5 minutes on a Pentium IV 1.8GHz Linux computer for a $400\times400\times60$ dataset that corresponds to a field of view of 18 μm laterally and 7.3 μm axially.

Reconstruction — Constrained iterative deconvolution

Although a constrained iterative deconvolution scheme is not necessary for SIM, it nevertheless has some potential in computationally enhancing the resolution and thus is worth investigating. In the iterative scheme, the gradient descent solution to minimizing Eq. 2.9 is used as follows:

$$\mathbf{d}^{(k+1)} = \mathbf{d}^{(k)} + \tau(-\nabla\Phi(\mathbf{d})) = \mathbf{d}^{(k)} + \tau \left(\sum \widehat{P}_i^t\widehat{\mathbf{b}}_i - \left(\sum \widehat{P}_i^t\widehat{P}_i + \lambda C^t C \right) \mathbf{d}^{(k)} \right).$$

At each iteration, the negative pixels of $f^{(k)}$ are set to zero. All the matrix multiplications (i.e., convolutions) are performed by multiplication in Fourier space.

The convergence of a gradient descent method is rather slow. By introducing a carefully chosen *preconditioner* Q [4, Sec. 5.5][7], the convolution equation can be modified to Qg = QPf without changing the solution to the original minimization problem, but the rate of convergence can be greatly improved.

2.3   Results

In this section, we will show SIM imaging results from experiments on various samples used for testing the performance of SIM. But first, the experimentally measured SIM OTFs are shown in Fig. 2.4. Fig. 2.4(a–c) correspond to order 0–2 of the SIM OTF (i.e., the $O_m(\vec{k})$'s for m=0–2 in Eq. 2.5) respectively. The steps involved in preparing radially averaged OTFs are detailed in Appendix B. These measured OTFs' support is mostly in agreement with the theoretical OTF support shown in Fig. 2.2. The only difference, as expected, is that order 1 and 2 OTFs are slightly broadened along k_z direction. This is caused by the finite area of the end face of the multi-mode optical fiber, as discussed at the end of Sec. 2.1.

Fluorescent microspheres

As a proof of principle, imaging was performed using samples of red fluorescent microspheres (121 nm in diameter, Molecular Probes, Eugene, OR), and the results are shown in Fig. 2.5. The microsphere suspension is diluted 1000 times and deposited on a cover slip. After it is dried, areas of densely packed multi-layer microspheres are formed. As seen from Fig. 2.5(a, c), two microspheres (pointed to by arrows) separated by 156 nm laterally, which is well below the resolution limit of the conventional microscope (Fig. 2.5(a)), can be clearly resolved with SIM (Fig. 2.5(c)). SIM's axial sectioning capability is demonstrated in Fig. 2.5(b, d). The out-of-focus glare from the 3D wide-field microscopy imaging (Fig. 2.5(b)) is mostly eliminated (Fig. 2.5(d)) because of the true sectioning capability of SIM. The full-width-at-half-maximum (FWHM) of the axial intensity profile through
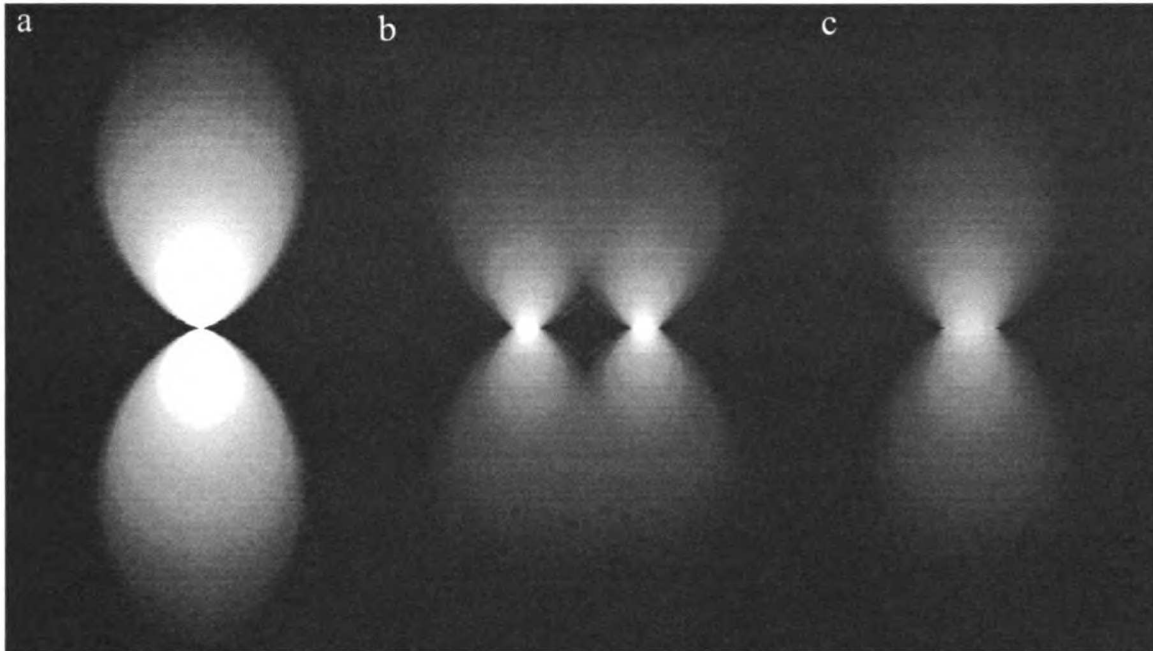
Figure 2.4: Experimentally measured and radially averaged SIM OTF. (a – c) are the O_m's for $m=0-2$ in Eq. 2.5 respectively. Vertical and horizontal directions correspond to k_x and k_z axes respectively. Images shown here are nonlinearly scaled (with $\gamma = 0.4$).

the center of a microsphere is 250 nm on average.

HeLa cell microtubules

HeLa cells were grown on cover-slips, fixed with glutaraldehyde, and then the microtubules were immuno-fluorescence labeled with primary (DM1A anti-α-tubulin, Sigma, St. Louis, MO) and Alexa Fluor 488-labeled secondary antibody conjugates (Molecular Probes) using standard protocols[2]. The fixed cells were then mounted in glycerol. Images were taken with SIM and reconstructed. Shown in Fig. 2.6(a) is the maximum-intensity projection of nine lateral sections from one such dataset. The two parallel microtubules pointed to by the arrows (Fig. 2.6(a) inset) are 125 nm apart (both of them are actually within a single lateral section before the projection). In the axial (x-z) view shown in Fig. 2.6(b), the distance between the arrow-pointed features is 360 nm. These numbers suggest that SIM has experimentally achieved the resolution limits that theory predicted. To demonstrate the potentials of SIM in structural biology, two stereo pairs of 3D volume rendering

---

[2]Mitchison laboratory protocols on fluorescence procedures for the actin and tubulin cytoskeleton in fixed cells (http://mitchison.med.harvard.edu/protocols/gen1.html)
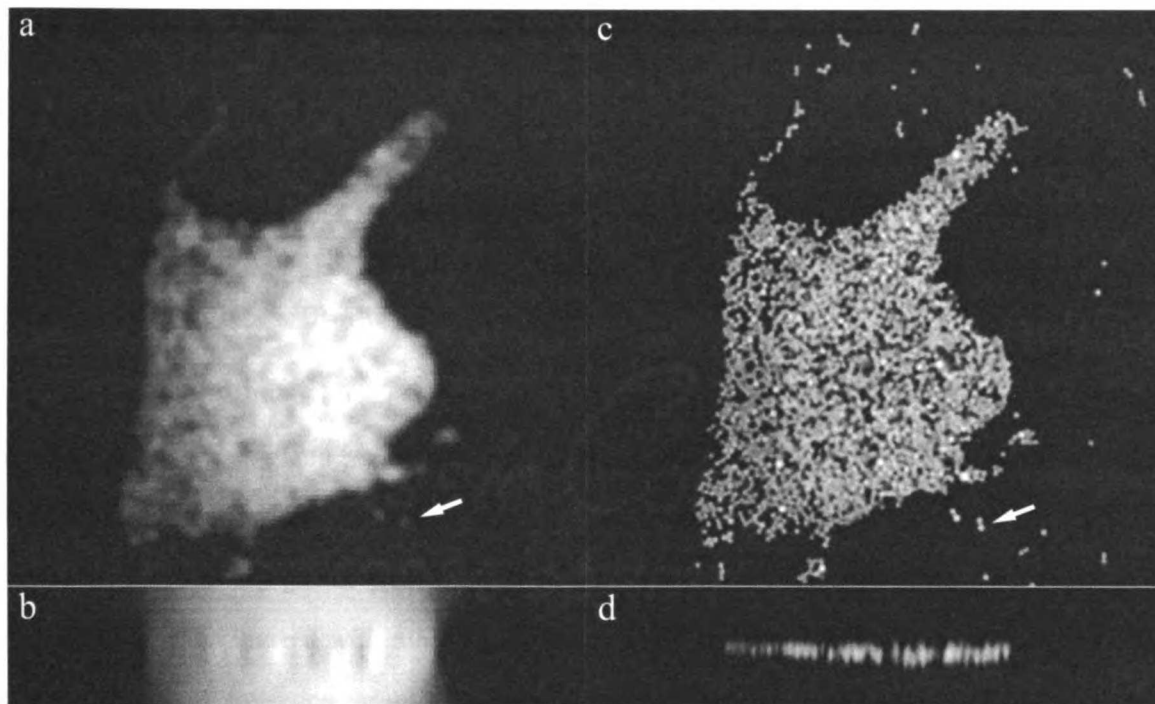
Figure 2.5: A comparison of resolving capability between conventional wide-field (a, b) and structured illumination (c, d) microscopy, both using the same sample made of red fluorescent microspheres of 121 nm diameter. In (a) and (c), one lateral (x-y) section from the 3D volume is shown. The arrows point to two beads 156 nm apart, which is well below the resolution limit of 220 nm of normal wide-field microscope at this wavelength. One cannot tell them apart in (a), but can do so with SIM (c). (b) and (d) show an axial (x-z) section of the volume. As can be seen, the optical sectioning capability with SIM is much better than the conventional microscope. The axial FWHM of a single bead is about 250 nm.

(maximum-intensity projected) of the same dataset, but from different viewing angles, are shown in Fig. 2.7.

Actin cytoskeleton

Mammalian cells of the HL-60 cell line were grown and induced to differentiate into neutrophil-like cells as described in [35], then briefly stimulated with their target chemoattractant, allowed to settle on cover slips, fixed with formaldehyde, labeled for actin with rhodamine phalloidin (Molecular Probes), and mounted in glycerol. The samples were then imaged with SIM and reconstructed. One example is shown in Fig. 2.8, in which the sample is around 12 μm thick, but the imaging quality was not compromised by the thickness.

Polytene puff-specific ssDNA-binding NonA protein

We imaged a DNA-binding protein, NonA [31], present in many puffs in polytene chromosomes of Drosophila salivary gland cells. This would further test the SIM's capability of handling optically highly heterogeneous samples such as polytene nuclei. NonA protein in our fly stock is tagged with GFP. The salivary glands were dissected from larvae, fixed with formaldehyde, mounted in glycerol, and then imaged with SIM. The reconstruction from one such dataset is shown in Fig. 2.9. In the lateral projection through the entire volume (Fig. 2.9(a)), one can see clusters of NonA molecules of similar size and shape, with each cluster presumably surrounding one puff along the polytene chromosomes. From the axial projections of several local regions (Fig. 2.9(b–d)), it is easier to appreciate the clustering since some clusters actually form a plane when viewed from certain angles. This experiment successfully demonstrates SIM's ability of dealing with thick and and optically heterogeneous biological materials.

Chromosomes of early-stage Drosophila embryos

Drosophila embryos of early stages (cycle 15 [10]) were high-pressure frozen, freeze-substituted with EGS acetone solution at liquid nitrogen temperature, then at room temperature placed in resin where acetone is gradually substituted with resin before the resin hardens into a plastic block. Each
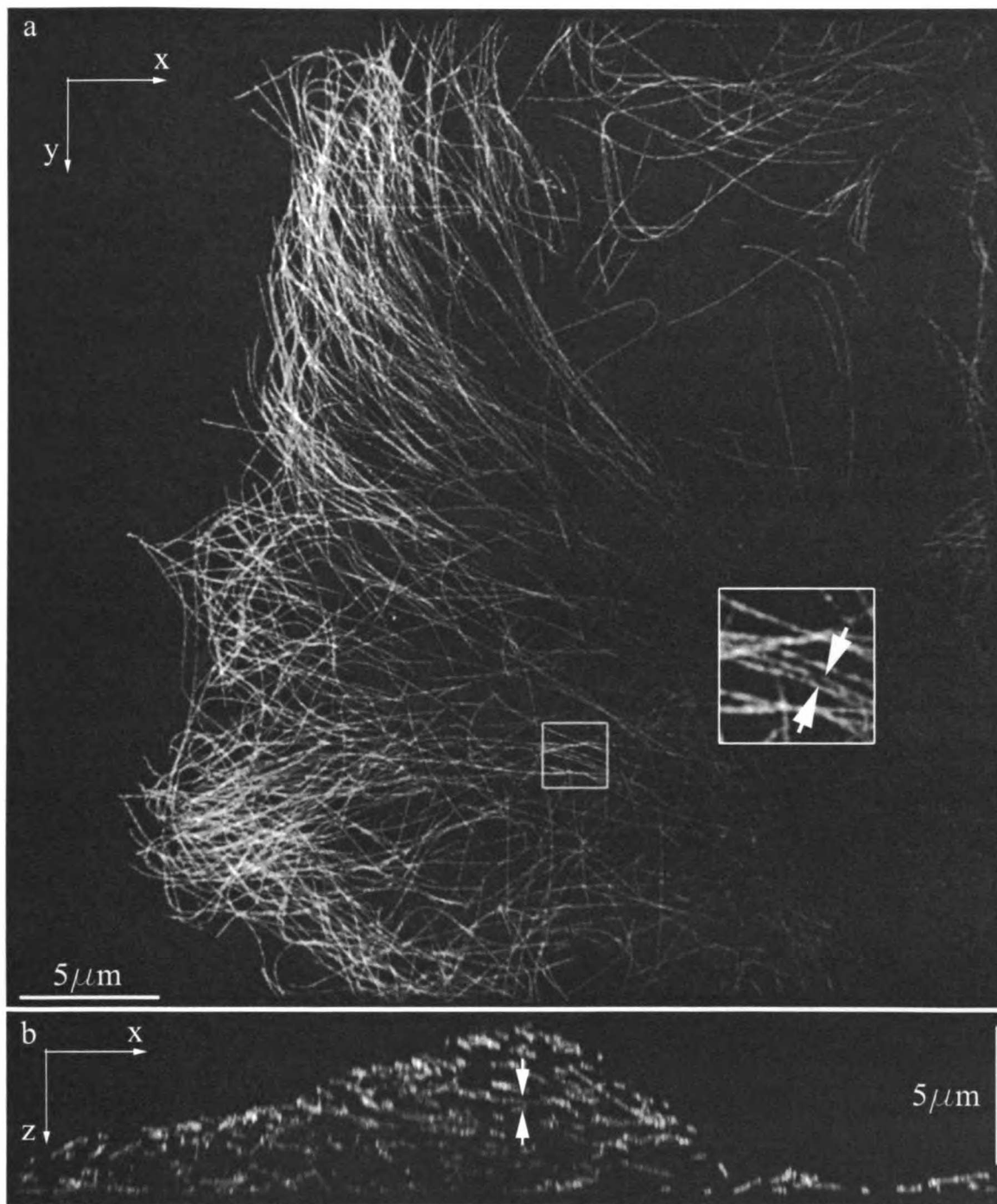
Figure 2.6: HeLa cell microtubules imaged with SIM. The lateral view (a) is a maximum-intensity projection through 9 lateral sections (about 1.1 μm in thickness) from a 3D volume, because in a single section microtubules are sparsely distributed. Inset: an enlarged sub-image enclosed with the small square, in which two parallel microtubule segments (pointed by arrows) are 125 nm apart and therefore could not be resolved with conventional microscope (data not shown). In the axial (x-z) view (b), the arrows point to two segments that are 350 nm apart axially, suggesting a much improved axial resolution of SIM.
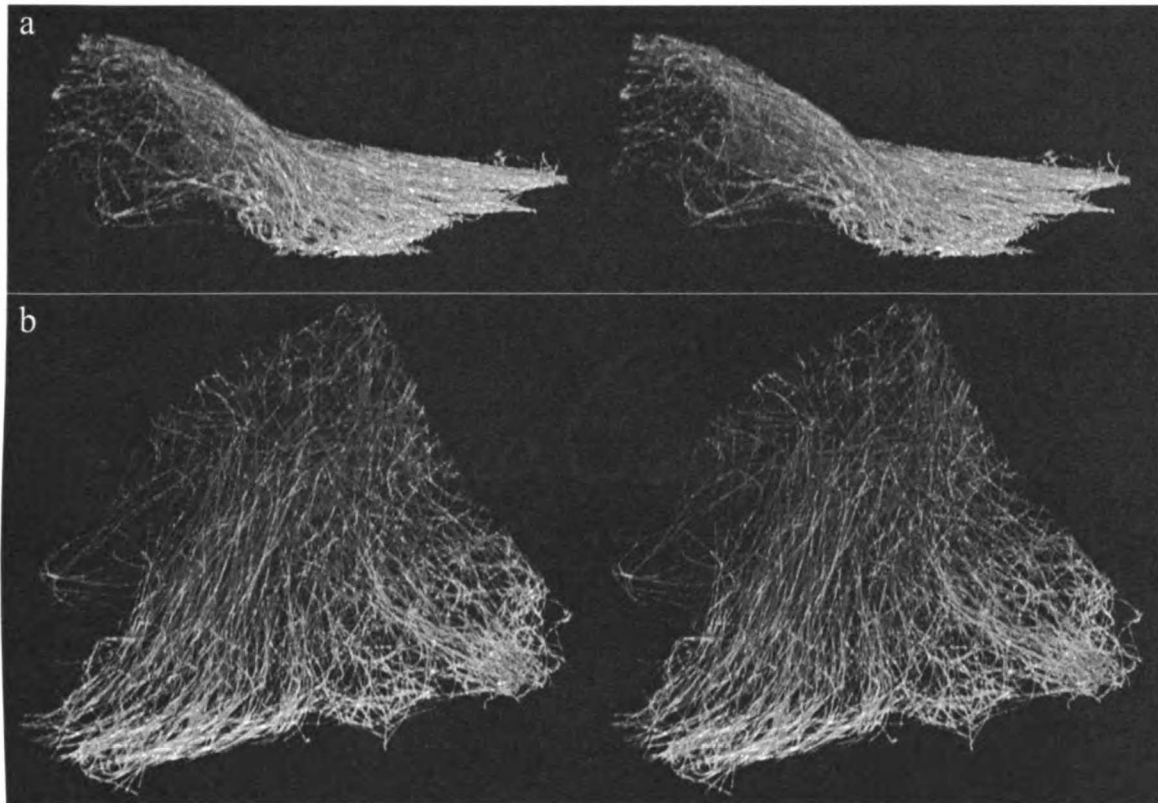
Figure 2.7: Two stereo pairs of maximum-intensity projected HeLa cell microtubules (the same dataset as in Fig. 2.6) to demonstrate the potentials of SIM in studying three-dimensional structural biology. In (a), a cavity corresponding to the nucleus can be easily appreciated in the stereo image.
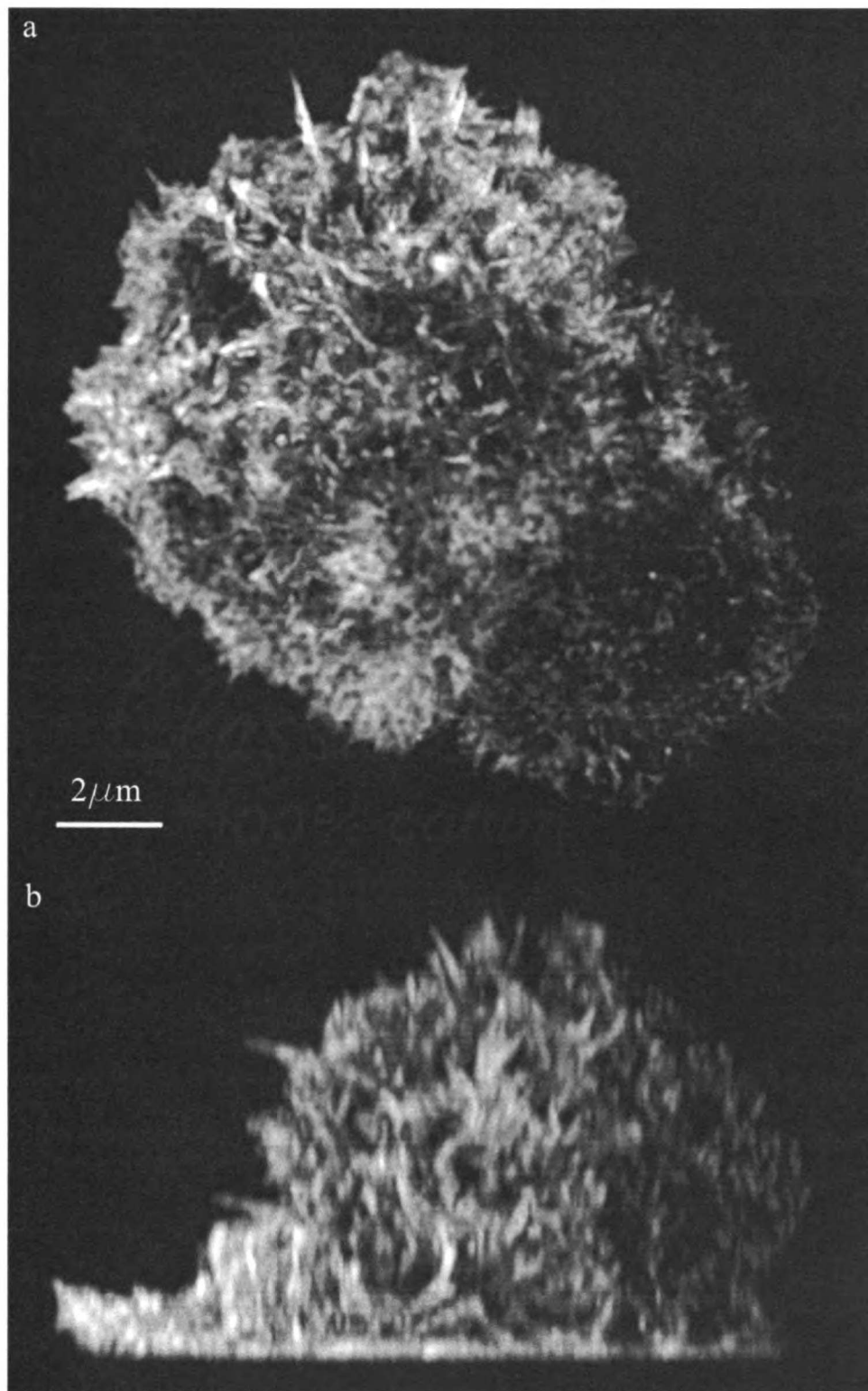
Figure 2.8: Maximum intensity projections through a 3D SIM reconstruction of the actin cytoskeleton in a human neutrophil-like cell, in top (x-y) view (a) and side (x-z) view (b).
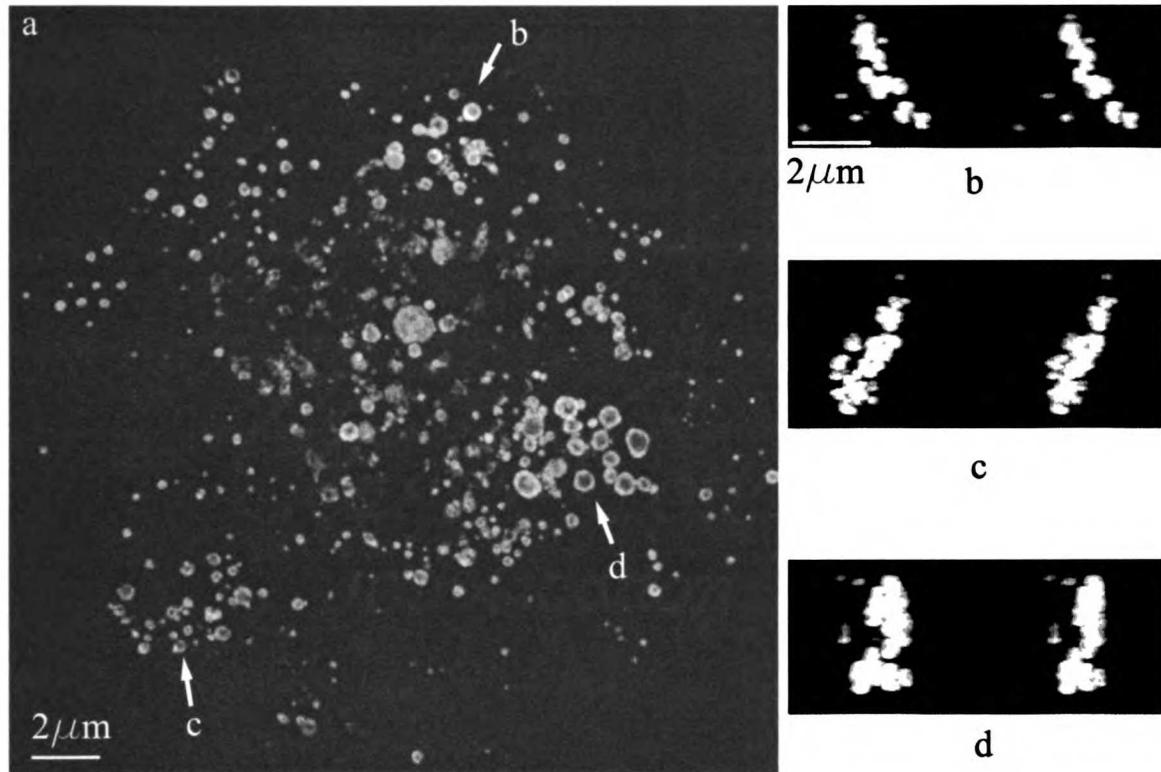
Figure 2.9: SIM images of GFP-tagged puff-specific NonA protein from salivary gland cells of Drosophila lavae. Shown in (a) is the projection through the entire 3D volume axially. One can notice clustering of the proteins of similar shapes and sizes (arrows in (a)) presumably surrounding puffs along polytene chromosomes. When viewed from other angles, the clusters pointed to by arrows b, c, and d (shown as stereo pairs of projection in (b), (c), and (d)) can be seen actually forming a plane that is probably normal to the chromosome axes.
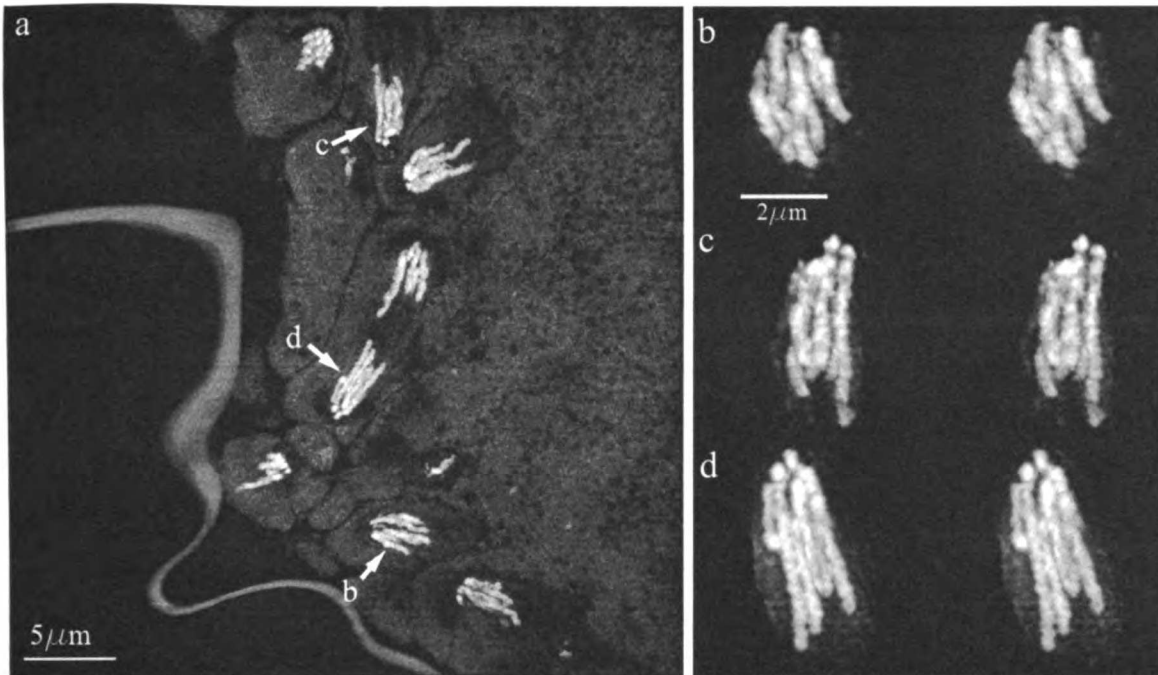
Figure 2.10: Cycle 15 Drosophila embryos were high-pressure frozen, freeze-substituted with EGS-acetone, and embedded in a resin block, which was then cut into 1 μm-thick sections as described in the text. The thin sections were then stained with OliGreen and imaged with SIM. Shown in (a) is the axial maximum-intensity projection of the entire volume reconstructed from such a dataset. (b–d) are stereo pairs of 3D volume projection of the nuclei pointed to by the arrows (b–d) in (a). Much greater details on the chromosomes can be appreciated from SIM images than from conventional images (data not shown).

resin block containing one embryo is cut into 1–2 μm sections [6]. The thin sections were then stained with OliGreen (Molecular Probes). We found that dye molecules penetrate the thin section acceptably when the section is immersed in the dye solution overnight. There are two reasons why we prepare the sample in such a complicated way. One is that high-pressure freezing is so far the best fixation approach for preserving sample structure. Second, the resin's refractive index matches very well with that of the immersion oil and aberration, both in illumination and detection, is therefore greatly minimized. Shown in Fig. 2.10 is a reconstructed SIM dataset taken for one embryo section sample thus prepared. All the nuclei in the field of view are undergoing anaphase. Great details along the chromosome arms can be appreciated (Fig. 2.10(b–d)). In a different plastic section sample where cells are in interphase (Fig. 2.11), SIM is able to reveal individual heterochromatin fibers in the axial view, thus providing the potential for the study of interphase chromosome organization, which to date is an extremely difficult problem to solve [26].
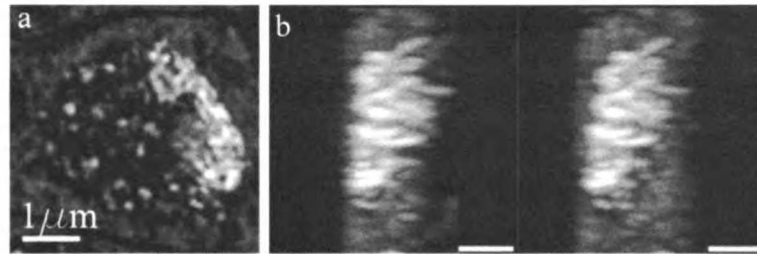
Figure 2.11: Interphase nucleus in one of the Drosophila embryo resin section samples reconstructed with SIM. Shown in (a) is the projection along z axis of the 3D volume and in (b) a stereo pair of side (y-z) projection view of the same nucleus. In (b), fiber-like structures, presumably heterochromatins, can be clearly traced. (All scale bars: 1.0 μm)

Mouse embryonic stem cell anaphase chromosomes

Mouse embryonic stem cells were grown on coverslips, fixed with EGS, stained with OliGreen, and mounted in glycerol. A mitotic cell in anaphase was imaged with SIM. In Fig. 2.12a, pictures of two selected lateral sections from the 3D SIM reconstruction are shown, in comparison with the corresponding sections observed from conventional microscope (Fig. 2.12b). One can see much more details along anaphase chromosomes in the SIM images. In Fig. 2.12c and d, an axial (y-z) cross-section of the same dataset is shown for SIM and conventional microscopy respectively. The axial resolution enhancement achieved with SIM is evident through this comparison. Finally, a particular chromosome arm is carved out and 3D rendered using maximum-intensity projection, as shown in Fig. 2.12e as a stereo pair.

S. pombe **mitotic chromosomes**

Fission yeast (*S. pombe*) cells were fixed with formaldehyde, treated with RNase, stained with OliGreen, deposited onto poly-L-lysine treated coverslips, and imaged with SIM. The yeast strain being imaged is nuc2 mutant [20]. nuc2 is a member of APC (anaphase promoting complex). The mutant is temperature sensitive and arrests at metaphase with short spindle at 36°C. Shown in Fig. 2.13 are two maximum-intensity projected stereo pairs of mitotic chromosomes from such a mutant arrested at metaphase. Considerable details can be noted.
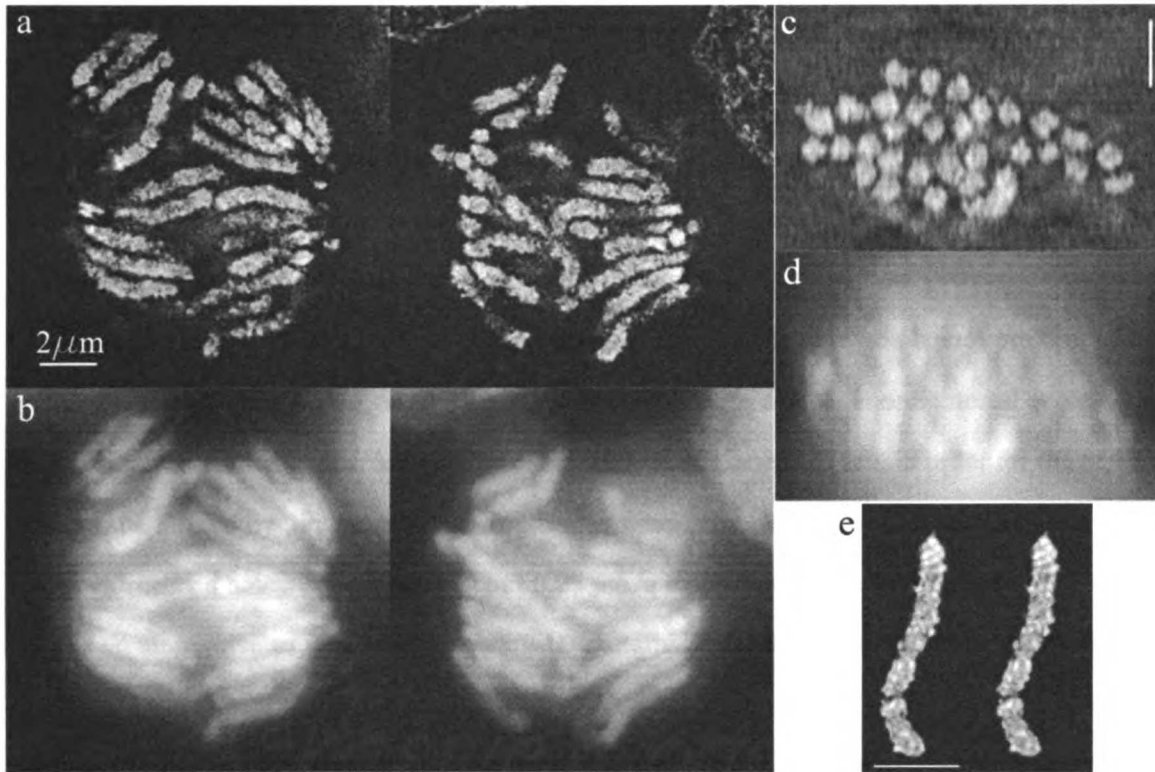
Figure 2.12: SIM images of mouse embryonic stem cell anaphase chromosomes. In (a) are two lateral sections from one dataset taken with SIM, and in (b) are the same sections viewed with conventional microscope. (c) and (d) are an axial (y-z) section of the same dataset, viewed from SIM and conventional microscope respectively. A particular chromosome arm was cut out and its 3D maximum-intensity rendering is shown in (e). (All scale bars: 2 μm)
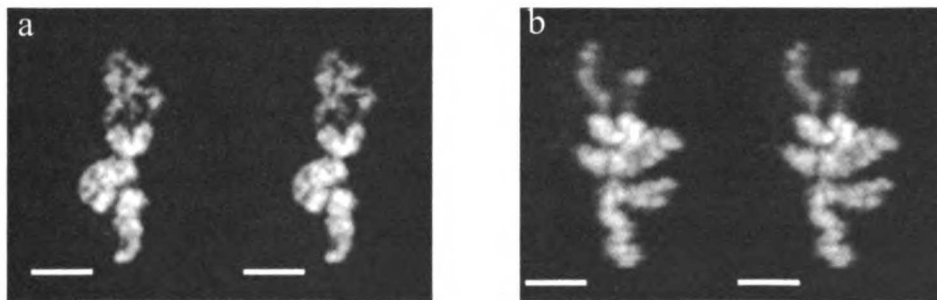
Figure 2.13: Stereo pairs of maximum-intensity projection of SIM images of S. pombe mitotic chromosomes. (All scale bars: 1 μm)

2.4 Discussion and Outlooks

There are several ways to generate structured illumination patterns besides the phase grating we used. For example, one can introduce interference by two or more laser beams. In our implementation, the grating is placed in a secondary image plane of the objective lens. One advantage of this approach is that the pattern is defined in essentially the "camera space" — the effective pattern as seen by the camera is geometrically perfect even if the objective suffers from geometric distortion. For the same reason, the phase of the pattern is stable as it is defined by the lateral position of the grating in camera coordinates, which are magnified relative to sample coordinates. For example, the grating would have to drift laterally by one period, in our case 33.5 μm, in order for the pattern phase to be altered by 2π; in an interfering-beams setup, any mirror could cause the same phase error by drifting a half wavelength, or about 0.25 μm, a much more likely occurrence.

As an alternative to repeatedly applying 1D patterns with different orientation, one can use a single, more complex 2D illumination pattern that contains structure in more than one direction, eliminating the need for rotation. A larger number of information components are then superposed in each image, so that a correspondingly larger number of images at different phases is required to separate them. The main drawback is that S-polarization cannot be achieved for all components simultaneously.

One factor that could limit the application of structured illumination microscopy to biology is sample thickness. It is well known that when imaging deep into sample, a microscope suffers spherical aberration because of the refractive index mismatch between the immersion medium and mounting medium/biological structure [24, 36]. For the same reason but in the opposite direction, the illumination pattern, when formed deep into the sample, would also be aberrated and become some structure different than expected, which makes it impossible to retrieve the high-resolution information. Another issue with thick sample is the much higher number of exposures. In our implementation, 15 exposures are taken for every focal section — 3 pattern orientations by 5 pattern phases. Hence a small increase in number of sections would multiply into a large increase in number of exposures and photo-bleaching then becomes a concern. The neutophil actin data demonstrates

that sample thickness of 12 μm can be handled very well by structured illumination microscopy. Most tissue culture cells grown on coverslips are within that thickness range. It could be, however, much more difficult to image cells inside tissues using this technique.

Live imaging with resolution beyond the diffraction limit would be much more attractive. Unfortunately that is not possible yet with the current SIM because the image reconstruction process assumes that the entire raw data represents a single, unchanging 3D structure, and the speed of data acquisition is simply not high enough to guarantee this assumption for live specimens that often undergo quite rapid motions and structural changes. Work is under way to investigate fast imaging techniques applied to SIM with the goal of SIM live imaging.

Chapter 3

I^5S

I^5S[1] is a second resolution enhancement scheme addressed in this thesis that integrates SIM with another interesting optical instrument — the interferometer, which comprises an array of detectors (such as lenses) and can generate fringes as a result of the interference effect. The astronomers have been using interferometer for resolution enhancement for more than a century [3]. The key to the idea is that the measured amplitude and phase of the interferometric fringes provides a direct measurement of the Fourier transform of the sky brightness distribution. For a given observing wavelength, the Fourier component measured is proportional to the separation of the interferometer elements (the baseline). These points form the basis of aperture synthesis imaging [33], in which combinations of various baselines are used in yielding an effective aperture much bigger than that of any single telescope, and thus a much improved spatial resolution. Today's average optical interferometer can accomplish a resolution roughly 100 times of that of the Hubble Space Telescope [3]. Fig. 3.1 demonstrates the principle of a two-element astronomic interferometer, with which I^5S shares many features. The two wavefronts collected independently by the two telescopes are delivered to a central beam-combining laboratory. In between the telescopes and the beam combiner, a delay-line made of movable trolleys holding mirrors is used for maintaining the optical path length equalization, a key condition for interference to occur at optical wavelengths.

The microscopy version of the interferometer [16] is limited by the feasible number of detecting

---

[1] I^5S stands for "Imaging Interference and Incoherent Illumination Interference with Structured illumination".

telescope

siderostat

secondary mirror

primary mirror
tip-tilt mirror

beam-combining laboratory

autoguiding system

CCD

mirror

beam-splitter

aperture
stop
filter
lens

APD 1

beam-combination
and interference
fringe detection

APD 2

trolley mirrors oscillate to
provide path-length modulation

trolley moves to maintain
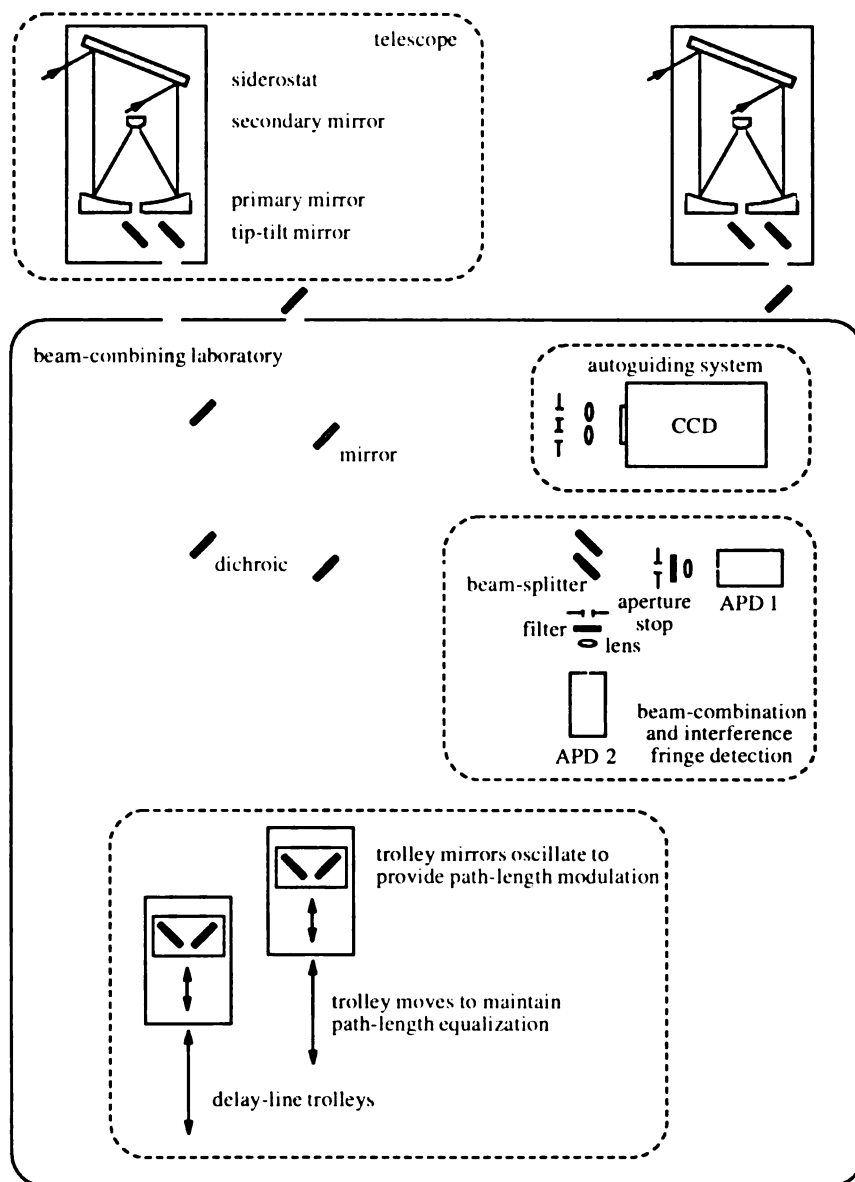path-length equalization

delay-line trolleys

Figure 3.1: A schematic view of a modern optical/infrared interferometer. Only two of the array elements (in this case siderostat-fed two-mirror telescopes) are shown here. CCD, charge-coupled device; APD, avalanche photo-diode. (Figure and caption reproduced from [3].)
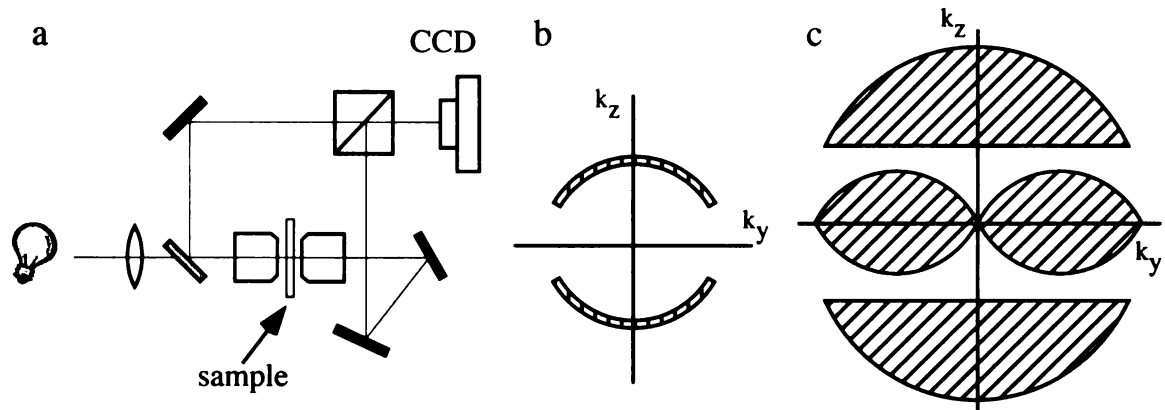
Figure 3.2: I²M (Image Interference Microscopy) is schematically shown in (a). The beam-splitter closest to the light source passes 20% and reflects 80% of the input light. The coherent detection of the emission light from both lenses amounts to the enlarged support of the generalized pupil function, as shown in (b), in comparison with normal one-lens microscope (Fig. 1.1). As a result, the support of the intensity OTF is extended axially (c), meaning better axial resolution.

elements, which is two because of the geometry of high-numeric aperture objective lenses and sample slides. Therefore, it cannot benefit from the phase closure [23] commonly used in astronomical interferometer for removing the phase error induced by atmospheric turbulence. Nevertheless, the basic principle of aperture synthesis was fully taken advantage of. In image interference microscopy, I²M [16], a fluorescent sample is mounted between two opposing objective lenses, each of which is focused on the same focal plane within the sample and forms a magnified image of this plane. These two images are combined by a beam-splitter and superposed on a single CCD camera (Fig. 3.2a). The optical path lengths of the two image beams are adjusted to be equal, causing the two beams of light from each fluorescent molecule to interfere with each other on the camera. In doing so, the overall aperture of the system becomes the union of the two objectives' aperture, as shown in Fig. 3.2b. The intensity OTF, which is the auto-correlation of the generalized pupil function [5], therefore has an axially extended support region compared to normal 3D OTF (Fig. 3.2c). The new frequency components that become observable are attributed to the axial interference fringes.

If in addition the excitation light is made to traverse the two paths and impinge on the sample through both lenses (Fig. 3.3), an axially varying illumination intensity is created through interference. In a manner similar to standing wave microscopy [2], this non-uniform excitation field modulates the pattern of emitted light and thereby encodes high-resolution axial information. We

Figure 3.3: I^5M schematic drawing. In addition to I^2M's (Fig. 3.2a), image interference, now there is also incoherent illumination interference (I^3) that gives rise to axial standing wave illumination pattern. That is, the I^2M PSF is further modulated by the illumination pattern. The combined effect is a better-than-100 nm axial resolution.

refer to this as "incoherent interference illumination" (I^3), since it uses an extended, spatially incoherent light source such as a standard arc lamp. The two kinds of interference are independent and can be used at the same time (I^5M [16]) to achieve a better than 100 nm axial resolution. With these previous work, including 3D SIM discussed in Ch. 2, already showing promising results, it is natural to ask the question whether one can apply structured illumination to I^5M and thereby obtain nearly 100 nm resolution in all three dimensions [17]. The rest of this chapter answers this question with the theory and experimental results of such a combined scheme, the I^5S microscopy. In a purely theoretical paper [12], a scheme called HELM was also proposed to generate both lateral and axial standing-wave illumination. But unlike I^5S, HELM does not include detection interference that can further enhance the axial resolution.

3.1 Concepts

To follow up the two previous resolution extension schemes, SIM and I^5M, we recently developed a new scheme, I^5S, that combines I^5M with lateral structured illumination and achieves a lateral and axial resolution as high as SIM and I^5M have achieved respectively. To do the combination, we simply replaced the conventional illumination apparatus of I^5M with that of the structured illumination and kept the interferometer of I^5M intact. Compared to I^5M, I^5S shares the same de-

tection OTF (i.e., I²M OTF, Fig. 3.4b), but is unique in its 3D, as opposed to I⁵M's 1D, standing-wave illumination pattern. And compared to 3D SIM, the illumination pattern of I⁵S contains more illumination components with higher axial frequencies (Fig. 3.4d). The pattern is generated through the interference of six coherent plane excitation wavefronts, three from each objective lens. The geometry of these wavefronts, represented in frequency space by their wave vectors $\vec{k}_i$, are shown in Fig. 3.4c. The two groups of three beams are symmetric with respect to the lateral (i.e., k_x–k_y) plane. Within each group, the two peripheral beams are both at an angle α off the center beam, which is coincident with the optical axis. The interference of these wavefronts gives rise to the 3D structured illumination pattern $I(\vec{r}) = \left| \sum_i \exp(j\vec{k}_i \cdot \vec{r} + \phi_i) \right|^2$ (scale factors are omitted herein), which, after some simplification based on the symmetry of $\vec{k}_i$'s, can be rewritten as a summation of 3 *orders* (denoted by m) of components:

$$I(\vec{r}_t, z) = \sum_{m=0}^{2} A_m(z) \cos(m\vec{k}_0/2 \cdot \vec{r}_t + \phi_m), \tag{3.1}$$

where $\vec{r}_t$ and z are the transverse and axial component of $\vec{r}$ respectively, $\vec{k}_0$ is the lateral difference vector between the 2 peripheral excitation wavefronts from one side of the sample (Fig. 3.4c) (i.e., through the same objective lens), and ϕ_m is the unknown phase of the lateral pattern of order m. Eq. 3.1 immediately reminds us of the form of a desirable illumination pattern discussed in Ch. 2 (Eq. 2.2). Within each order, the illumination is the multiplication of a lateral sinusoidal pattern, whose line spacing and orientation are determined by $m\vec{k}_0/2$, multiplied with an axial sinusoidal pattern encapsulated in $A_m(z)$. The Fourier transform of $I(\vec{r}_t, z)$ can be intuitively represented by the dots in frequency space shown in Fig. 3.4d, each corresponding to one sinusoidal component in Eq. 3.1. These components fall into 3 lines, or orders, parallel to the k_z axis based on whether their lateral distance from the k_z axis is 0, $|\vec{k}_0|/2$, or $|\vec{k}_0|$. It follows that if a 1D function is plotted versus k_z along each of these lines, we would get $\tilde{A}_m(k_z)$, the Fourier transform of $A_m(z)$.

We now examine how the structured illumination pattern $I(\vec{r})$ functions in extending the effective OTF support in I⁵S. When $I(\vec{r})$ illuminates some sample with a 3D structure $D(\vec{r})$, the fluorescent emission from sample layer z is $D(\vec{r}_t, z)I(\vec{r}_t, z')$. Different axial coordinates are used for $D(\vec{r})$ and $I(\vec{r})$ because the illumination pattern is stationary while the sample moves axially relative to the optical system (the second condition for SIM discussed on page 9). An arbitrary coordinate system

can be used for $I(\vec{r})$ as long as it's stationary relative to the microscope. For convenience, the PSF's coordinate system is chosen to overlap with $I(\vec{r})$. The recorded 2D image when layer z of $D(\vec{r})$ is in focus is thus given by the convolution integral:

$$G(\vec{r}_t, z) = \iint D(\vec{r}_t - \vec{u}, z - v)I(\vec{r}_t - \vec{u}, v)P(\vec{u}, v)\,\mathrm{d}\vec{u}\mathrm{d}v, \tag{3.2}$$

where $P(\vec{u}, v)$ is the 3D I^{2}M PSF since the detection of the emission is done as in I^{2}M. We can then substitute (3.1) into (3.2), and since integral and summation are interchangeable, we have

$$\begin{aligned}G(\vec{r}_t, z) &= \sum_{m=0}^{2} \iint D(\vec{r}_t - \vec{u}, z - v)\cos(m\vec{k}_0/2 \cdot (\vec{r}_t - \vec{u}) + \phi_m)A_m(v)P(\vec{u}, v)\,\mathrm{d}\vec{u}\mathrm{d}v \\ &= \sum_{m=0}^{2} \left(D(\vec{r}_t, z)\cos(m\vec{k}_0/2 \cdot \vec{r}_t + \phi_m)\right) \otimes (A_m(z)P(\vec{r}_t, z)). \end{aligned} \tag{3.3}$$

Therefore, raw data of I^{5}S is the superposition of 3 orders of data, each of which is a convolution of two parts: 1) the sample structure modulated by a purely lateral pattern; and 2) the I^{2}M PSF modulated by a purely axial pattern. In frequency space, Eq. 3.3 becomes

$$\widetilde{G}(\vec{k}_t, k_z) = \sum_{m=0}^{2} 0.5\left(\widetilde{D}(\vec{k}_t - m\vec{k}_0/2)e^{-j\phi_m} + \widetilde{D}(\vec{k}_t + m\vec{k}_0/2)e^{j\phi_m}\right)O_m(\vec{k}), \tag{3.4}$$

where $O_m(\vec{k})$ is the Fourier transform of $A_m(z)P(\vec{r})$, the effective OTF of order m. With Eq. 3.4 it is now obvious how resolution extension is realized in I^{5}S. First, as in I^{5}M, OTF support is extended axially by the convolution of detection OTF, $O(\vec{k})$, with $\widetilde{A}_m(k_z)$, which contains a series of delta functions along the k_z direction (Fig. 3.4(d)). Second, as in 2D and 3D structured illumination, the sum in Eq. 3.4 suggests that the raw data contains sample frequency spectra laterally shifted by a displacement vector $\pm\vec{k}_0/2$ or $\pm\vec{k}_0$, indicating some normally unobservable sample information becomes effectively accessible to the microscope. Taking these two aspects into account would yield the effective OTF support of I^{5}S shown in Fig. 3.4e.

In order to extract the five components that make up the summation (3.4), five images need to be acquired using the same illumination pattern with different lateral phases ϕ_m. Five linear equations, with the five components as unknowns, are thus generated and can be easily solved. As in 3D SIM, two more 3D image stacks are needed with the lateral pattern rotated around the optical axis to two other orientations 60 and 120 degrees from the first one. Overall, the shape of I^{5}S OTF support is a nearly isotropic sphere (Fig. 3.4f), with doubled and 7-fold extension in lateral
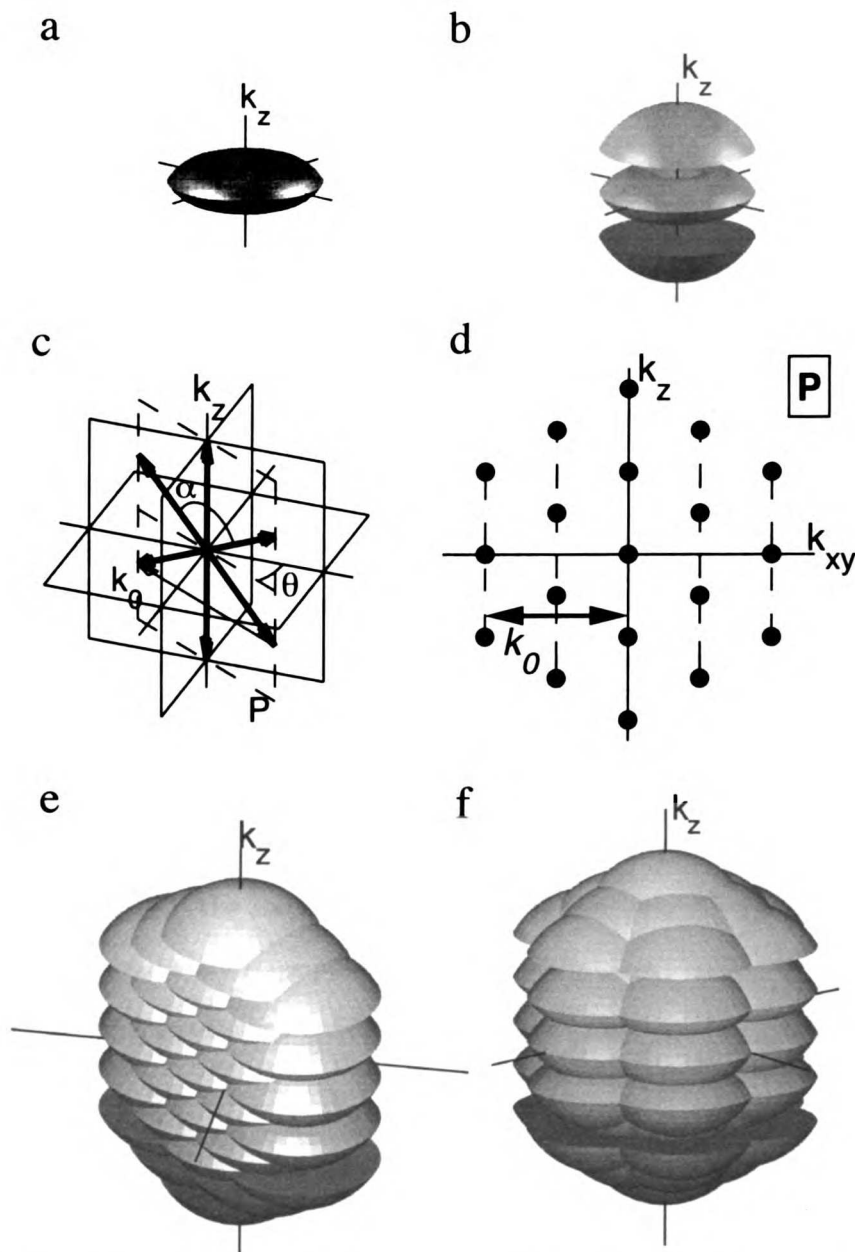
Figure 3.4: (a) and (b) are the support of a conventional wide-field OTF and I^5S detection (i.e., I^2M) OTF, respectively. In (c), the six vectors in plane P of frequency space represent the excitation wavefronts. Shown in (d) are the frequency components of the illumination pattern as a result of the interference of the six wavefronts. The horizontal axis here is the intersection of plane P and $k_x - k_y$ plane in (c). (e) is the effective OTF support using the illumination pattern shown in (d). After two other pattern orientations, i.e., angle θ in (c), are applied, the overall effective OTF support of I^5S is nearly a sphere as shown in (f).

and axial direction respectively compared to the OTF support of conventional wide-field microscope (Fig. 3.4a).

3.2 Implementation

3.2.1 Optomechanical setup

A prototype I^5S system was built to demonstrate its resolving power. As shown in the schematic drawing (Fig. 3.5), two features distinguish I^5S from the conventional wide-field microscope. The first, as in I^5M [16], is the amplitude-splitting interferometer consisting of a beam splitter and two identical optical paths. Each path consists of a pair of metallic mirrors and an oil-immersion objective lens (Nikon PlanApo, NA 1.4, 100×, 160 mm conjugate). The illumination wavefronts are split into two halves by the beam splitter, each taking one path of the interferometer to reach the sample. The two halves of emission wavefronts, collected by the two lenses, are combined by the beam splitter. Optics in one of the two paths (the stationary path) are fixed relative to the optical bench. In the other path (the movable path), the lens and the pair of mirrors are mounted on a 3-axis and 1-axis translational stage respectively, both controlled by close-loop nano-positioning system (Queensgate Instruments, Torquay, UK). The 3-axis stage allows precise alignment between the two lenses in all three directions, and the 1-axis stage precise control of the path length difference between the two optical paths. The other essential part of I^5S is the structured illumination setup. Please refer to Sec. 2.2.1 for the detail.

3.2.2 Image acquisition and reconstruction

I^5S image acquisition is performed in mostly the same manner as in SIM (Sec. 2.2.2), but with a smaller z step size (36.6 nm as opposed to SIM's 120 nm) because of the much improved axial resolution. The major difference of I^5S imaging, however, lies in the stringent requirements on the imaging conditions, which include the three-dimensional alignment between the two objectives and the equalization of the optical path length of the two paths in the interferometer. Before one starts the automated data taking, a series of alignment steps have to be done as follows:
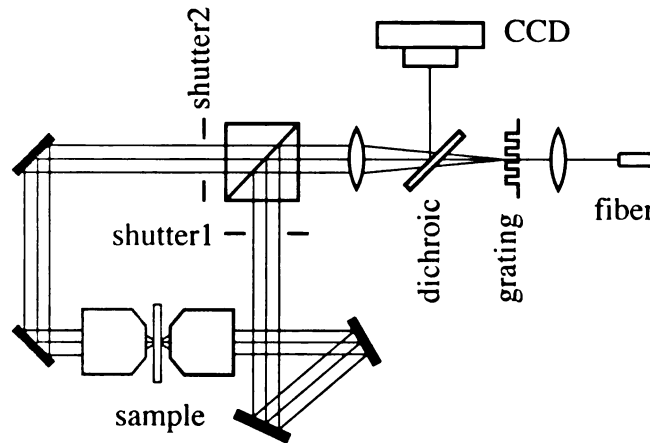
Figure 3.5: The schematic drawing of I^{5}S setup (only the chief illumination rays are shown for all three diffraction orders). The mirrors and objective lens in blue are in the movable path — the objective lens is mounted on a XYZ stage and the two mirrors are together mounted on a one-dimensional translational stage, both stages close-loop controlled to move with nanometer precision.

1. Adjust the sample stage so that an arbitrary point-like object in the sample is in focus with respect to the stationary objective;

2. Make the movable objective also focus on the same point source by adjusting the z axis of the movable objective stage;

3. Make the movable objective laterally align with the stationary one by comparing two images taken with either shutter 1 or 2 open;

4. With both shutters open, plot a curve of the intensity of the point object's center against the optical path length of the movable path, which can be controlled by the piezoelectric stage where the movable mirrors are mounted, and set the mirror stage to the position corresponding to the peak of the curve;

5. Again with both shutters open, plot a curve of the intensity of the point object's center against the focal position of the sample and adjust the stage until one obtains a symmetric profile so as to make the peak of the PSF and the interference fringes overlap.

The above steps usually have to be iterated several times as the alignment done minutes earlier could have changed slightly by the time one starts, say, step 5. Once the above steps have been done, one can proceed with data taking throughout which the carefully obtained alignment state

must be maintained via additional mechanisms as discussed in Appendix C.

Image reconstruction for I^{5}S uses exactly the same procedure as that for SIM.

3.3 Results

3.3.1 Measured I^{5}S OTF

Single fluorescent microsphere of 50 nm in diameter was used to measure the I^{5}S OTF. A normal I^{5}S dataset is taken on the bead with just one lateral pattern orientation. This dataset, an I^{5}S PSF, is then processed and radially averaged as discussed in Appendix B. The amplitudes of the OTFs thus obtained are shown separately for each order in Fig. 3.6. The phases of the OTFs (not shown) are another key attribute in I^{5}S imaging, as they vary with the path length (or phase) difference of the interferometer.

3.3.2 Beads cluster

To demonstrate the resolution of I^{5}S, we used test samples made of a stack of red-emission fluorescent beads (FluoSpheres, Molecular Probes) of 121nm in diameter. A drop of diluted beads suspension was deposited onto a cover-slip and then dried on a slide warmer. The cover-slip was then covered with another smaller cover-slip using microscope immersion medium (Laser Liquid, Cargille Labs, Cedar Grove, NJ) as mounting medium. The smaller cover-slip was sealed against the larger one with nail polish. Fig. 3.7 shows images taken on such sample with either I^{5}S or the same microscope working in conventional wide-field mode. The comparison between Fig. 3.7(a, c) and (b, d) clearly demonstrates that I^{5}S resolution is much superior to conventional 3D wide-field microscope. In fact, it can easily resolve objects 0.15 μm apart laterally (Fig. 3.7(c)) and 0.12 μm apart axially (Fig. 3.7(d)). This same sample was also imaged with SIM (Fig. 2.5). The stack of beads unresolvable axially (Fig. 2.5d) under SIM can be clearly seen as layers under I^{5}S (Fig. 3.7c arrow).
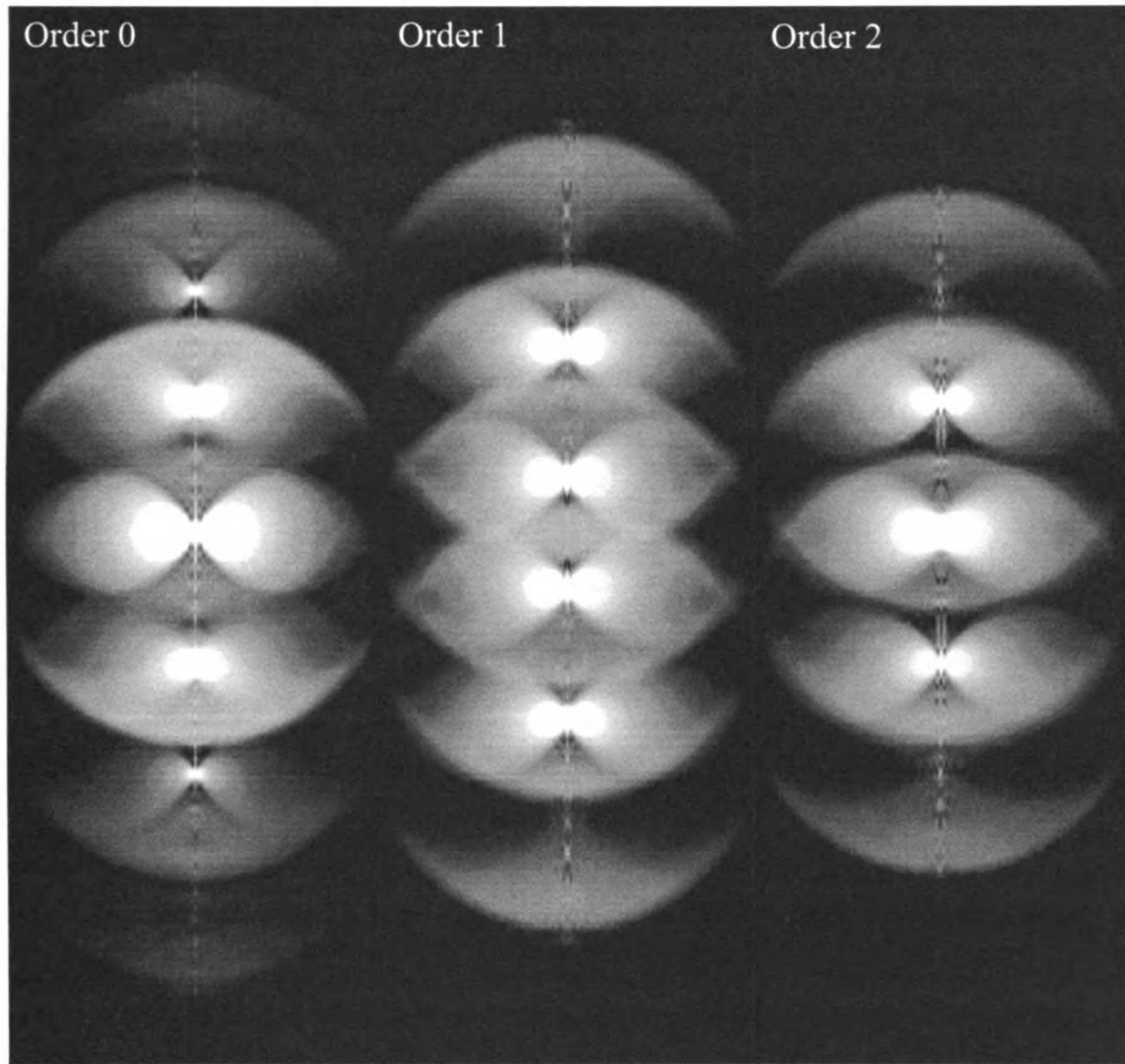
Figure 3.6: Experimentally measured and radially averaged I^5S OTF of order 0, 1, and 2. Only the amplitude is shown.
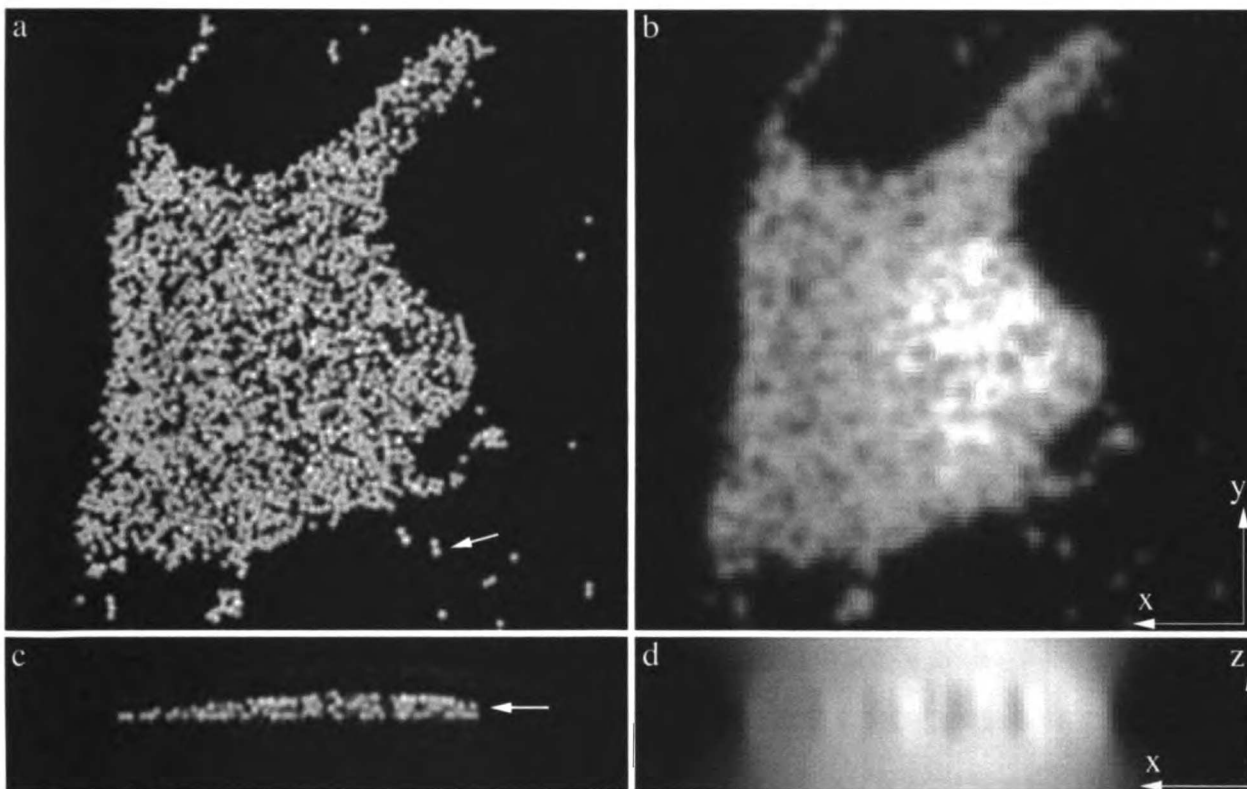
Figure 3.7: I^5S reconstruction of fluorescent beads cluster sample, in comparison with a normal 3D microscope image. One lateral and axial section from I^5S reconstruction are shown in (a) and (c) respectively. (b) and (d) are the corresponding sections seen from a normal 3D wide-field microscope. The two adjacent beads pointed to by an arrow in (a) are 158 nm apart from center to center, which are not resolvable in (b). In (c), the arrow points to two layers of beads that are 120 nm apart.

3.3.3 HeLa cell microtubules

Biological samples were also used for testing I^5S. One type of sample is HeLa cell microtubules. HeLa cells were grown on coverslips and then fixed using standard protocol as mentioned in Sec. 2.3. The fixed cells were then stained with anti-α-tubulin primary antibody (DM1A, Sigma) and then Alexa488 labeled secondary antibody (Molecular Probes). Since I^5S used oil-immersion lenses, the aqueous environment inside the cells changes the path length difference between the two optical paths of the interferometer as the sample moves axially during data acquisition. This can seriously alter the axial phase of the interference fringes, one essential imaging condition, from section to section and render invalid the LSI 3D imaging model that we assumed. Therefore the sample has to go through further steps in an attempt to optically homogenize the interior of the cells.

We found that the immersion medium we used, Laser Liquid made by Cargille, has two useful properties: it doesn't reduce the fluorescence intensity of the dyes immersed in it and it intermixes with acetone. With these in mind, we developed the following protocol to exchange the water inside the fixed cell with Laser Liquid. The fixed and stained sample was crosslinked again in 4% formaldehyde before it was stepped through a series of acetone-water mixture, 5 minutes for each step, with increasing acetone concentration from 20% to 100%. The sample was thus dehydrated after water-acetone exchange. Next, the sample was stepped through a series of acetone-Laser Liquid mixture with increasing Laser Liquid concentration from 20% to 100% and ready for imaging. Shown in Fig. 3.8(a) is the maximum-intensity projection of a part of the reconstructed 3D volume from one such experiment. The vertical surface on the right (or y-z plane) intersects the cell's nucleus that appears as a cavity in the volume rendering and is surrounded by a highly dense meshwork of microtubules. As can be seen, the 3D structure of the cytoskeleton is successfully delineated by I^5S. Fig. 3.8(b) shows a portion of one lateral (x-y) section, where two adjacent microtubules 120nm apart can be seen resolved. Axial resolution of 90nm is demonstrated in Fig. 3.8(c).

3.3.4 Meiotic chromosomes of *C. elegans*

The other type of sample used for I^5S is meiotic chromosomes in *C. elegans* gonad. A special protocol [9] was used for handling the worms since it is notoriously difficult to fix and stain. In
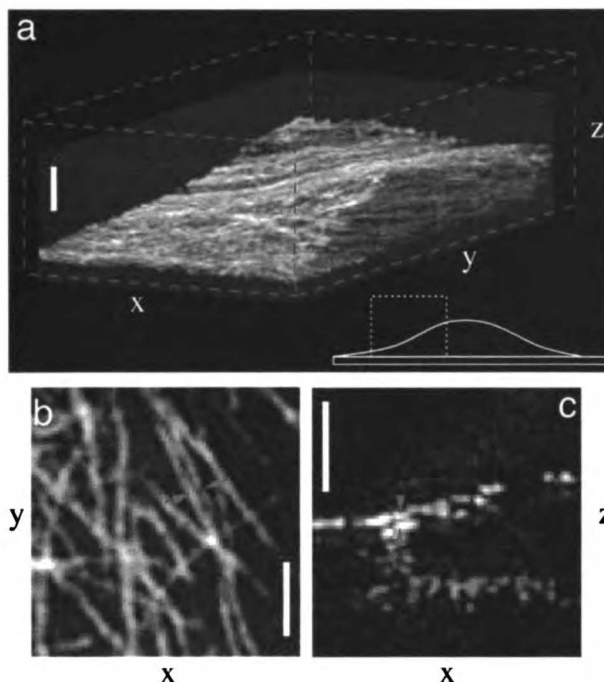
Figure 3.8: HeLa cell microtubule imaged with I^5S. (a) Volume rendering of the 3D data. (b) and (c) are small portion of a lateral and axial section respectively. In (b), the separation between the two parrallel microtubules pointed to by arrows is 120nm. In (c), the separation is 90nm. (All scale bars: 1.0 μm)

brief, the hermaphrodite worm was high-pressure frozen at liquid nitrogen temperature and freeze-substituted with EGS acetone solution. Then at room temperature the sample was placed in resin, in which it went through acetone-resin substitution before resin hardened into a plastic block. Later the block was cut into 2.5 μm slabs that contain the portion of the gonad with germ cells in the pachytene stage. Samples prepared this way not only avoid the difficulty in penetration of chemicals into the worm, but also the resin's refractive index matches the immersion medium very well — another way of achieving optically homogeneous samples. Incidentally, high-pressure freezing also excels at preserving structures. The thickness of 2.5 μm of the slabs was chosen such that fluorescence dye can still fully penetrate the plastic. For staining, the slabs were immersed in OliGreen (Molecular Probes) solution overnight. Results show that staining went well using this procedure (Fig. 3.9(c, d). The stained slabs were then mounted in between two cover-slips with Laser Liquid as the mounting medium. Shown in Fig. 3.9 are examples of reconstructed images acquired on the slabs sample. It is noticeable that not only are chromosomes stained, but also in cytoplasm and nucleolus as
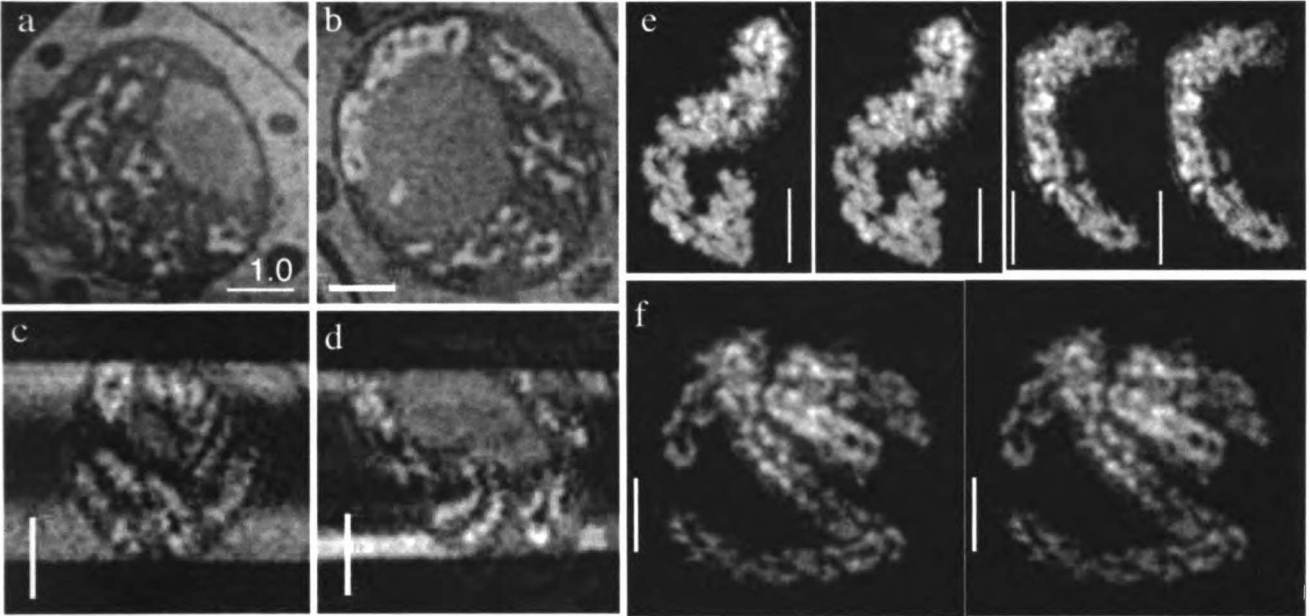
Figure 3.9: C. elegans meiotic chromosomes. (a) and (b) are lateral sections cutout from the I^5S reconstruction. Not only the chromosomes, but also the nucleoli and cytoplasm are visible because the fluorescence dye also stains RNA. (c) and (d) show two examples of axial sections. The voids seen outside the nuclei are due to incomplete dye penetration. In (e), two stereo pairs of volume rendered individual chromosomes are shown. (f) is another stereo pair showing the conformation of several chromosomes.

OliGreen can stain RNA as well. The meiotic chromosomes are seen localized to the periphery of the nucleus wrapping around the nucleoli with approximately the same high resolution in both lateral (Fig. 3.9(a, b)) and axial sections (Fig. 3.9(c, d)). The stereo pair projections of individual (Fig. 3.9e) and a congregation of chromosomes (Fig. 3.9f) demonstrates the usefulness of I^5S in the study of structural biology at 100 nm resolution level. The 3D chromosome structures seen from I^5S definitely display more complicated features than the conventional view of homolog configuration at the pachytene stage of meiotic prophase [32].

3.4 Discussion and Outlooks

To ascertain the theoretical resolution limit of I^5S, we want to first obtain the reconstructed image of an ideal point source (or rPSF — reconstructed PSF) in the following way. The image of an ideal point source is simulated by multiplying 1 with the I^5S OTF everywhere in frequency space. The rPSF can then be obtained by doing reconstruction on the simulated raw image. Two rPSF's

are then superposed with a distance in between. The resolution limit is therefore the smallest such distance when the two points can still be resolved under Rayleigh's criterion. The results indicate that I^5S has a lateral and axial resolution limit of 110 and 90 nm, respectively, when the emission wavelength is around 515nm and excitation wavelength is 457nm.

In comparison with other schemes that utilizes axial illumination and detection interference, I^5S is unique in that the residual axial ringing pattern can be fully removed in the final reconstruction. This feature is due to the LSI imaging model that I^5S is based on — however much ringing is present in the raw image data, it is but a convolution of the object with the PSF. As long as the PSF or OTF is well-conditioned, which is the case for I^5S (see below), a simple linear deconvolution (or inverse filtering in frequency space) can then remove the ringing patterns. Therefore, purely computational post-processing as opposed to other complicated optical schemes is sufficient for obtaining ringing-free reconstruction. The LSI imaging model does, however, imply that imaging condition of the data shall match that of the PSF/OTF. A key imaging condition for I^5S is obviously the phase of the axial interference fringes, determined by the path length difference between the two branches of the interferometer. To keep this condition (we normally choose 0 path length difference, i.e., total constructive interference) from changing as a result of remounting samples, it is essential that before each experiment one must conduct routine check on it as described in section 3.2.2. To do this, we plot the image intensity of some axially point-like object versus the changing path length difference and then use the phase stage position corresponding to the peak from then on. The pre-experiment preparation also includes aligning one objective lens with the other laterally and making them confocal. Overall, 15-20 minutes of preparation is necessary before each experiment.

The LSI imaging model used by I^5S imposes a limitation on sample preparation when oil-immersion lenses are used — the sample's refractive index has to match that of the immersion oil. This requirement is not as stringent for 4Pi-confocal microscopy since deconvolution is not essential there. In that case one can control the phase stage during data acquisition so as to compensate the phase change induced by refractive index mismatch [34]. This approach is not directly applicable to I^5S since even though phase change is removed, the degree of spherical aberration varies from section to section. That is, the condition for using the LSI model is still unmet. Neither of the two

approaches we used for obtaining matched index of the sample (see Sec. 3.3) is totally satisfactory. Oil-acetone-water exchange tends to flatten the cells, and embedding cells in plastic is tedious and sometimes poses an extra barrier for dye molecule penetration. For I^5S to better suit biological applications, it might be worth compromising the resolution slightly by using lower NA glycerol- or water-immersion objective lenses.

The success of linear deconvolution used in I^5S depends on how well-conditioned the PSF or OTF is. An OTF is ill-conditioned if there are "gaps", or zero-valued patches, inside its overall support. Linear deconvolution is unable to recover information missing in those gaps and the reconstruction contains ringing artifacts. For I^5S, the factor determining whether or not the OTF is well-conditioned is the incident angles of the peripheral excitation wavefronts (i.e., the angle α in Fig. 3.4c). This is because 1) these angles determine the distribution of the illumination harmonic components' distribution in frequency space (Fig. 3.4d), and 2) the effective OTF can be considered a convolution of these components with the detection OTF (Fig. 3.4b). When α is about 60°, which approaches the acceptance angle for a NA 1.4 oil immersion lens, the illumination components are evenly distributed and there is no gap in the effective OTF support (Fig. 3.10a), i.e., the OTF is well-conditioned. Results shown earlier were all obtained under such condition. This condition can not be met simultaneously for different excitation wavelengths because the diffraction angle is wavelength dependent. For example, if α is 60° for 532nm laser, then it becomes 55° for 488nm laser line. An I^5S OTF taken at this condition is shown in Fig. 3.10b, which contains gaps and is therefore ill-conditioned. Different magnifying lens in front of the grating has to be used for each illumination wavelength so as to keep α at 60°.

The excitation wavefronts were S-polarized (parallel to the grating direction) in order to maximize the interference fringes' modulation depth. S-polarization was maintained regardless of the grating's orientation around the optical axis as the polarizer was made to co-rotate with the grating. However, the beam-splitter cube, an essential part of I^5S, introduces different phase delay for vertically and horizontally polarized wavefronts. As a result, a linearly polarized wavefront will become elliptically polarized after it passes the beam splitter unless it is vertically or horizontally polarized. An elliptically polarized excitation wavefront reduces the modulation depth of the illumination pat-
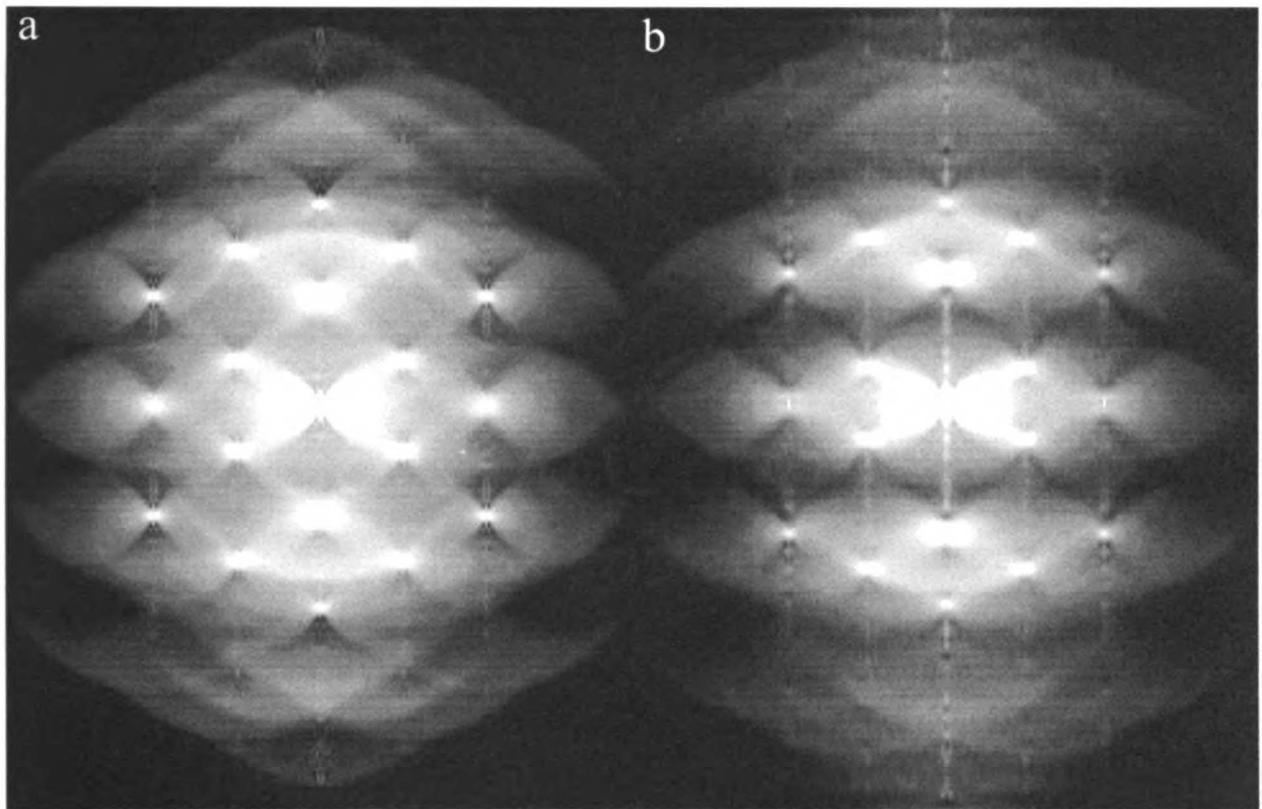
Figure 3.10: The measured and assembled I^5S OTFs. Different orders of OTF is prepared as described in Sec. 3.3. An assembly of these OTF components produces these overall OTF images. (a) and (b) were taken when the peripheral excitation wavefront's incident angle was $60°$ and $55°$ of respectively. It can be seen that (b) contains more low-intensity gaps than (a).

tern and is therefore undesirable. Since three orientations of the illumination pattern are used for I^5S, at least one orientation's S-polarization angle is close to neither horizontal nor vertical direction, in which case the ellipticity of the excitation's polarization is the most severe. However, our experiments showed that the modulation depth even in the worst case proves to be sufficient for generating the desired extended-resolution information.

Chapter 4

I^{5}S with Dual Image Interference Detection

One element is clearly missing from the interferometer setup of I^{5}S shown in Fig. 3.5 — the fluorescence signal coming out of the north port of the beam-splitter cube is discarded. In this chapter, we address the question whether I^{5}S can be further improved if that signal is captured and made useful. We will first discuss the phase relationship between the signals from the east (main) and north (auxiliary) port of the cube. Based on this relationship, we will then develop a method with which the path length inequality (or axial phase error) in the interferometer can be estimated from I^{5}S image data detected through both ports. The estimated phase error can then be taken into account in the image reconstruction to reduce the axial ringing artifacts, a result of not taking action against the phase error. Single-bead imaging results are presented at the end to support the validity of the theory. If proven feasible experimentally, such a scheme can relax the requirement on the accuracy of path length equalization prior to each experiment.

4.1 Complementary phase

In our implementation the I^{5}S interferometer is aligned in such a way that the two fluorescence wavefronts, one from each path, constructively interfere at the main exit port of the beam-splitter.
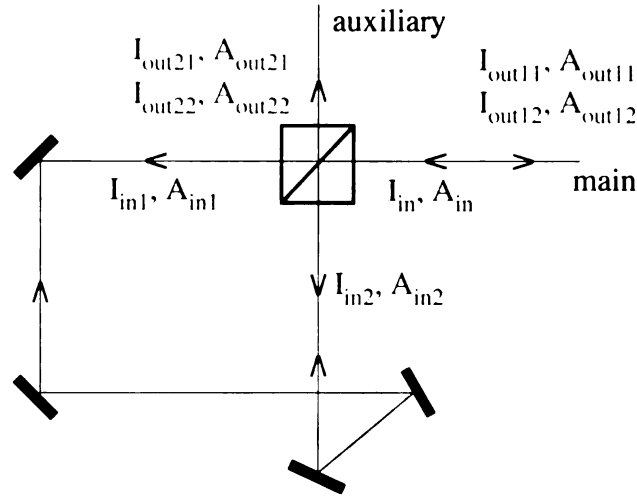
Figure 4.1: The reason we should see destructive interference at the auxiliary exit of the beam-splitter when constructive interference occurs at the main exit. Drawn here is almost an exact copy of I⁵S interferometer except without the objectives. Suppose a beam with intensity $I_\text{in} = 1$ (amplitude $A_\text{in} = 1$) is the input to the interferometer, and after the beam-splitter each path get a half of the energy ($I_\text{in1} = I_\text{in2} = 1/2, A_\text{in1} = A_\text{in2} = 1/\sqrt{2}$). Each half gets split after they pass the beam-splitter again on the way out. Ignore the interference effect for the moment and we have for the main exit $I_\text{out11} = I_\text{out12} = 1/4, A_\text{out11} = A_\text{out12} = 1/2$ and for the auxiliary exit $I_\text{out21} = I_\text{out22} = 1/4, A_\text{out21} = A_\text{out22} = 1/2$. If the interferometer is aligned in such a way that constructive interference happens at the main exit, the intensity there would be $I_\text{out1} = (A_\text{out11} + A_\text{out12})^2 = 1$. By means of energy conservation, this means that the two wavefronts at the auxiliary exit must undergo destructive interference such that $I_\text{out2} = (A_\text{out21} - A_\text{out22})^2 = 0$.

It can be shown (Fig. 4.1) that under this circumstance, the two fluorescence wavefronts undergo destructive interference at the auxiliary exit port. This relationship can be further generalized into the following statement: if the phase difference between the two interfering wavefronts at the main exit is φ, then that difference at the auxiliary exit would be $\varphi + \pi$. We can prove this statement simply by using the fact that the intensity at the main exit is $I_\text{out1} = I_\text{out11} + I_\text{out12} + A_\text{out11} A_\text{out12} \cos \varphi$ [5, Sec. 7.2], given the phase difference φ between the two output beams at the main exit. Since $I_\text{out11} + I_\text{out12} = I_\text{in}/2$ and $I_\text{out21} + I_\text{out22} = I_\text{in}/2$, it is mandatory that the phase difference at the auxiliary exit be $\varphi + \pi$ so that $I_\text{out1} + I_\text{out2} = I_\text{in}$, i.e., energy conservation.

What this relationship means for I⁵S is rather interesting. Recall the I²M (i.e., I⁵S detection) concept figures (Fig. 3.2) for a moment. The phase difference of φ between the two exit wavefronts, at either exit port, tranlates into a φ phase difference between the top and bottom shell in the generalized pupil function (OTF$_\text{A}$) of I²M (Fig. 3.2b). Since the OTF is an auto-correlation of OTF$_\text{A}$, the three parts of the OTF support, from the top to the bottom in Fig. 3.2c, have a phase of φ, 0,

and $-\varphi$, respectively. Therefore between the two OTF's obtained at the main and the auxiliary exit, there exists a π phase difference in the top and bottom parts of the OTF support and 0 in the central part. Since an image in frequency space is a point-wise multiplication of the object's spectrum and the OTF (Eq. 1.1), the point-wise π phase shift relationship also holds between two datasets' Fourier transform of any sample taken through the two different exits. In other words, the addition (or subtraction) of these two datasets's Fourier transform, which exhibits the same non-zero regions as an I^2M support, produces a result with only the central (or top and bottom) region of the detected spectrum being non-zero, provided that a correct scaling has been applied. The significance of this statement will become clear at the end of the next section.

4.2 Phase difference estimation and compensation

In I^5S or any other interferometric instruments, a big challenge is how to achieve path length equalization. (The maintenance of the equalization (see Appendix C) is another big issue for three-dimensional microscopy because it takes tens of minutes to collect one dataset, but is assumed a given condition in this chapter.) As mentioned in the previous chapter, a significant amount of time needs to be spent on digitally adjusting the path length of the movable path of the interferometer before each experiment in order to achieve zero path length difference between the movable and the staionary path. In fact, this requirement is not really necessary as long as the path length difference when acquiring a dataset is the same as that when acquiring the OTF being used for reconstruction. In either case, a specific value of path length difference has to be reached. Otherwise, it is highly likely that the OTF used for reconstruction does not match the dataset in path length difference and thus the reconstructed results exhibit axially ringing artifacts (Fig. 4.2). Therefore to relax the requirement on path length equalization without suffering from ringing artifacts, so as to make I^5S easier to use, the path length (or phase) difference needs to be estimated from each dataset. With this quantity known, one can then either choose from a library of OTF's a matching one or, in a more attractive solution, synthesize an OTF that can account for the estimated phase difference and reconstruct with this OTF. OTF synthesis will be the topic of Sec. 4.3.
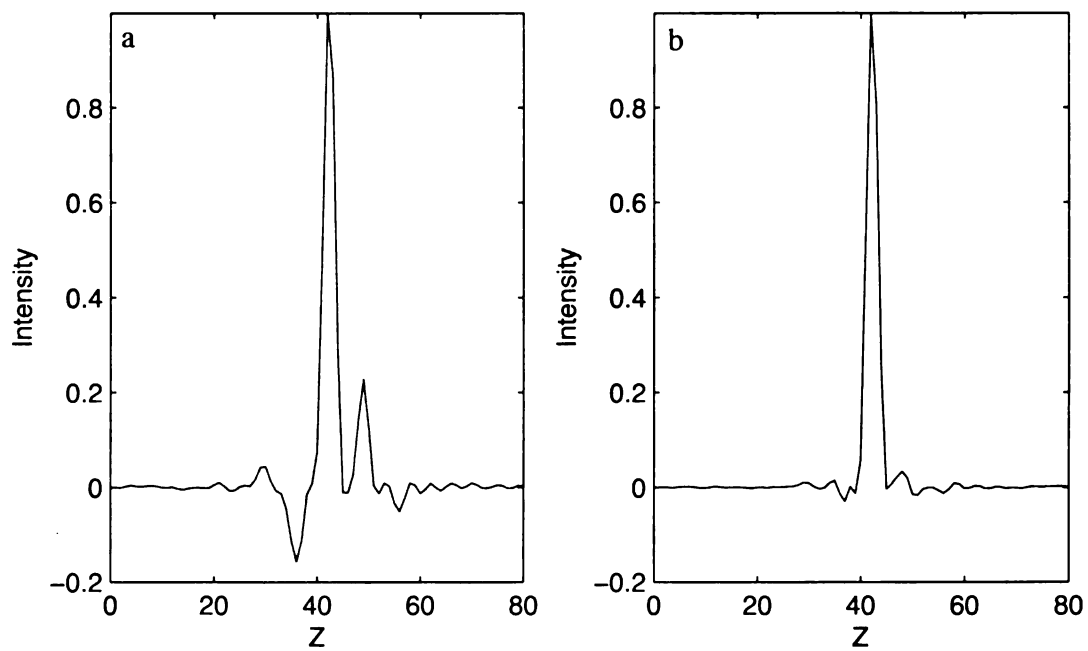
Figure 4.2: Reconstruction using an OTF not matching the dataset in terms of path length difference results in (a), which shows axial intensity profile through the center of a point source. When a matching OTF is applied for reconstructing the same dataset, the result suffers much less from axial artifacts as shown in (b). (Intensity values are normalized relative to the maximum intensity.)

The effect of phase difference on I^5S data

Before developing a scheme for phase difference estimation, we first need to find out what is expected about the phase in a I^5S OTF given a known path length difference δ. As shown in Fig. 4.3a, the detection OTF is divided into three regions with distinct phase values of b, 0, and $-b$, where $b = 2\pi\delta/\lambda_{em}$. These values are attributed to the fact that the detection OTF is an auto-correlation of the generalized pupil function (OTF$_A$, Fig. 3.2b), and the relative phase difference between the two shells making up OTF$_A$, i.e., the two wavefronts collected separately by the two objectives, is b. Similarly for the illumination harmonic components (Fig. 4.3b) generated by the interference of the six coherent excitation wavefronts, three groups can be distinguished based upon the components' phase, which can be a, 0, and $-a$, where $a = 2\pi\delta/\lambda_{ex}$. The reason is that the phase of the three illumination wavefronts from one objective is a relative to that of the three wavefronts from the other objective. From Eq. 3.4 we already know that there are three orders of OTF for I^5S, each being a convolution of the detection OTF and one of the three illumination orders (Fig. 3.4d and 4.3b). The color-coded maps of phase in these OTF orders are shown in Fig. 4.3(c-e). Because in convolution phases of the operands add, the phases in different regions of I^5S OTF are various additive combinations of 0, $\pm a$, and $\pm b$.

Phase difference estimation

We should recall that an I^5S dataset consists of three 3D volumes, each of which acquired with a different lateral illumination pattern orientation. Each volume is first separated into five information components (Tab. 2.1), each of which is a portion of the sample spectrum filtered by the corresponding order of OTF. As a result, the OTFs' phase map is added to that of the sample's spectrum. In reality, different orders of information components are not isolated, but partially overlay with each other. For example, the dashed line in Fig. 4.3d should coincide with the dashed line in Fig. 4.3c because of the lateral spectrum shift that the order 1 components have undergone. This is the key to our scheme of estimating the phase difference in I^5S. If we place order 1 components at their correct spatial location, as illustrated in Fig. 4.4, we find that the green colored sub-component of order 1 partially overlaps with the red colored sub-component of order 0 (both sub-components
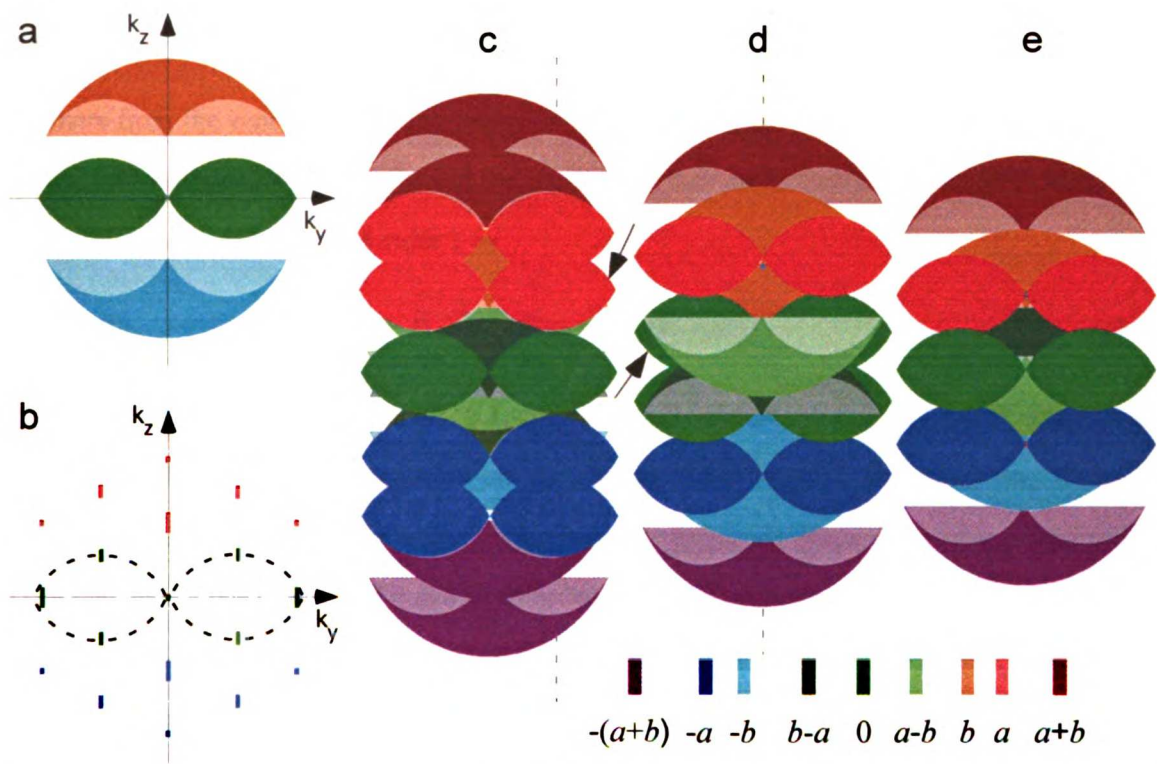
Figure 4.3: Color-coded phase map of I²M OTF (a), I⁵S illumination structure (b), and I⁵S OTFs of all three orders (d–e).
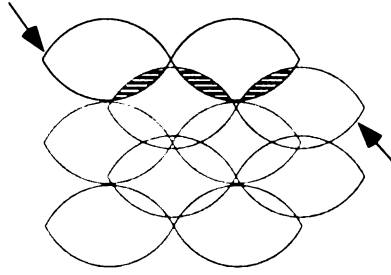
Figure 4.4: Illustration of overlaps between order 0 and 1 components. A portion of the order 0 and 1 components shown in Fig. 4.3(c, d) are reproduced here, with order 1 placed at the correct spatial location. The arrows of Fig. 4.3(c, d) are also copied here, pointing to the same sub-components. The partial overlaps between the sub-components are highlighted by the hatched regions. For clarity only the central sub-components are drawn.

originate from the central part of the detection OTF support (Fig. 3.2c) and will be referred to as central sub-components herein). Within the overlap, the raw data's Fourier transform at frequency $\vec{k}$ of order 0 is related to that of order 1 by

$$\widetilde{B}_0(\vec{k})O_1(\vec{k}) = e^{ja}\widetilde{B}_1(\vec{k})O_0(\vec{k}),\tag{4.1}$$

where $\widetilde{B}_0$ and $\widetilde{B}_1$ were defined in Tab. 2.1, and O_1 and O_2 are the order 0 and 1 OTF respectively, as defined in Eq. 2.3. Linear regression can then be applied to solve Eq. 4.1 for a using all points within the overlap. This means it is straightforward to estimate the phase difference a, from which b can then be deduced, provided that a clean overlap between *only* the two central sub-components pointed to by arrows in Fig. 4.3 is obtainable. Unfortunately, on top of those two central sub-components are superimposed other sub-components (originating from the top/bottom portion of the detection OTF support , referred to as axial sub-components herein) that have different phases. Consequently, the linear relationship of Eq. 4.1 does not hold true any longer between any order 0 and 1 point $\vec{k}$ within the overlap.

This is where the conclusion of Sec. 4.1 comes into play. If fluorescence emission from both of the beam-splitter exits are recorded at the same time as shown in Fig. 4.5, then the summation of these two correlated image datasets' Fourier transform contains only the central sub-components and the subtraction the axial sub-components. The sum may then be used in place of the normal dataset recorded through the main exit for extracting the overlap shown in Fig. 4.4. In this case, the overlap is not contaminated by the axial sub-components and therefore Eq. 4.1 can be employed in
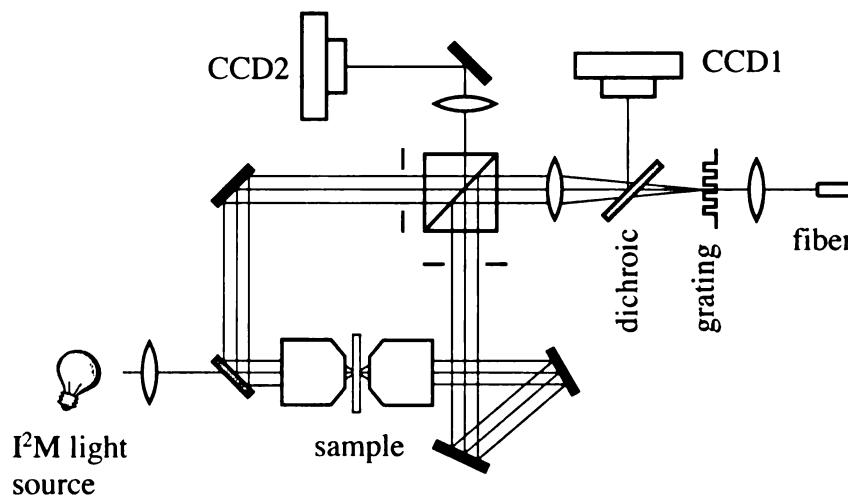
Figure 4.5: The expansion of the I^5S setup to include the second detection path. The CCD and the relay optics on the second path is made to duplicate the main path as closely as possible. The lower left mirror partially transmitts so that one can use the setup to take I^2M dataset if needed (see Sec. 4.3).

estimating a more accurately.

Before the summation and subtraction are performed, the image pairs recorded on the two CCDs have to be carefully aligned. There exists some unavoidable residual misalignment between each pair even with the two CCDs already physcically aligned as precisely as can be achieved by mechanical means with the system shown in Fig. 4.5. The residual misalignment, mainly due to 2D translation and rotation, can be calibrated with scatter beads images. The result of the calibration, a 2D affine transform matrix, can then be saved for aligning the image pairs in all subsequent experiments.

4.3   OTF synthesis based on the estimated phase difference

Given the estimated phase difference, we need a scheme to apply this information to the image reconstruction process. One scheme is to have a library of OTFs taken with varying phase differences, from which an OTF is then chosen that corresponds to the estimated phase difference. Though straightforward, such a scheme requires a specific path length difference to be realized before every experiment (in this case OTF acquisition), the same kind of difficulty that we wish to overcome from the beginning of Sec. 4.2, and therefore this is not an attractive solution. Here we introduce a more

flexible scheme built upon the fact that I⁵S OTFs are the convolution of the detection (or I²M) OTF $O(\vec{k})$ with one of the one-dimensional axial illumination structures $\tilde{A}_m(k_z)$ of Eq. 3.4. If somehow the measured I⁵S OTF can be decomposed into $O(\vec{k})$ and $\tilde{A}_m(k_z)$'s, then once the phase difference is estimated from a dataset one can easily apply the phase to $O(\vec{k})$ and $\tilde{A}_m(k_z)$ by multiplying $\exp(ja)$ or $\exp(jb)$ to the right parts of $O(\vec{k})$ or $\tilde{A}_m(k_z)$ according the phase map (Fig. 4.3(a, b)). Next, the phase-adjusted $O(\vec{k})$ and $\tilde{A}_m(k_z)$'s can be convolved to synthesize the OTFs that will then be used to correctly reconstruct the dataset.

OTF separation

In order to separate I⁵S OTFs into two convolving components, one of the components has to be known. Fortunately we can measure I²M OTF at the same time an I⁵S is being measured, provided that the lower-left mirror in Fig. 4.5 also transmits partially (20% is what we use) such that a conventional illumination path can be set up to the left of that mirror. Shutter control chooses between conventional and structured illumination path.

The OTF separation problem is formulated as solving for $\tilde{A}_m(k_z)$ in $O_m(\vec{k}) = \tilde{A}_m(k_z) \otimes O(\vec{k})$ given $O_m(\vec{k})$ and $O(\vec{k})$. Since $\tilde{A}_m$ is a one-dimensional function, this problem is equivalent to solving it in a series of 1D deconvolution problems

$$O_m(k_z, \vec{k}_t) = \tilde{A}_m(k_z) \otimes O(k_z, \vec{k}_t) \tag{4.2}$$

for each point $\vec{k}_t = (k_x, k_y)$ in the Fourier space's lateral dimension. As we always average 3D OTF around the k_z axis (see Appendix B) into a 2D representation OTF$_{ra}$ that has an axial and a lateral axis, Eq. 4.2 becomes

$$\mathbf{O}_{m,n} = \tilde{\mathbf{A}}_m * \mathbf{O}_n, \tag{4.3}$$

in which we use vector notations, $*$ is the linear discrete convolution operator, and $\mathbf{O}_{m,n}$ and $\mathbf{O}_n$ represent column n of mth-order I⁵S and I²M OTF$_{ra}$, respectively. A linear convolution can be transformed into a circular convolution, which can then be formulated as a vector being multiplied by a cyclic matrix, if the vectors have a sufficiently short support or are padded with enough zeros [4, Sec. 2.7]. The advantage of converting Eq. 4.3 into a cyclic matrix multiplication format is that the 1D deconvolution problem can be converted into a least-squares problem as shown below.

Suppose the length of each vector in Eq. 4.3 is N, and the middle point of the vectors corresponds to $k_z = 0$, and the 0th and the $(N-1)$th element of the vectors correspond to $k_z = -K/2$ and $K/2$ respectively, where K is the axial sampling frequency we used in data taking. The nth column vector of I^2M OTF_{ra}, $\mathbf{O}_n$, is first shifted by $N/2$ and denoted as $\overline{\mathbf{O}}_n$. A cyclic matrix is then constructed from $\overline{\mathbf{O}}_n$ as follows [4, Sec. 2.5]:

$$O_n = \begin{bmatrix} \overline{\mathbf{O}}_{n,0} & \overline{\mathbf{O}}_{n,N-1} & \overline{\mathbf{O}}_{n,N-2} & \cdots & \overline{\mathbf{O}}_{n,1} \\ \overline{\mathbf{O}}_{n,1} & \overline{\mathbf{O}}_{n,0} & \overline{\mathbf{O}}_{n,N-1} & \cdots & \overline{\mathbf{O}}_{n,2} \\ & & \cdots & & \\ \overline{\mathbf{O}}_{n,N-1} & \overline{\mathbf{O}}_{n,N-2} & \overline{\mathbf{O}}_{n,N-3} & \cdots & \overline{\mathbf{O}}_{n,0} \end{bmatrix}$$

Then Eq. 4.3 can be rewritten as $\mathbf{O}_{m,n} = O_n \widetilde{\mathbf{A}}_m$. Multiple such equations for all the columns of $\mathbf{O}_m$ and I^2M OTF_{ra} can then be stacked to form an over-determined equation

$$\underbrace{\begin{bmatrix} \mathbf{O}_{m,0} \\ \mathbf{O}_{m,1} \\ \vdots \\ \mathbf{O}_{m,N-1} \end{bmatrix}}_{\dot{\mathbf{O}}_m} = \underbrace{\begin{bmatrix} O_0 \\ O_1 \\ \vdots \\ O_{N-1} \end{bmatrix}}_{\dot{\mathbf{O}}} \widetilde{\mathbf{A}}_m. \tag{4.4}$$

$\widetilde{\mathbf{A}}_m$ in Eq. 4.4 can then be easily solved with least-square solution

$$\widetilde{\mathbf{A}}_m = (\dot{\mathbf{O}}^* \dot{\mathbf{O}})^{-1} \dot{\mathbf{O}}^* \dot{\mathbf{O}}_m,$$

where $\dot{\mathbf{O}}^*$ is the hermitian conjugate of $\dot{\mathbf{O}}$.

OTF synthesis

Once the solutions of the axial illumination structures $\widetilde{\mathbf{A}}_m$ for all three orders are found, they are permanently stored together with the measured I^2M OTF_{ra} $\mathbf{O}$. When it is time to reconstruct a dataset, the excitation phase difference a is first estimated as discussed in Sec. 4.2. The emission phase difference b is simply $a(\lambda_{ex}/\lambda_{em})$. The top and bottom regions of the detection OTF support are multiplied by e^{ja} and e^{-ja} respectively, and the red group of components of $\widetilde{\mathbf{A}}_m$'s shown in Fig. 4.3b are multiplied by e^{jb} and the blue group by e^{-jb}. To synthesize OTFs that best account for

the imaging condition of the dataset, one just needs to convolve the phase-adjusted O and $\tilde{A}_m$'s. The synthesized OTF is then used in reconstructing the normal I^5S dataset acquired from the main beam-splitter exit.

4.4 Results

OTF separation

Fig. 4.6 shows the result of separating I^5S illumination structure from a measured I^5S OTF as discussed in Sec. 4.3. The three curves in Fig. 4.6(A–C) are the amplitude of I^5S illumination structure versus k_z in the frequency space for order 0, 1, and 2 respectively.

Complementary phase relationship

A pair of I^5S PSFs were taken simultaneously from the two CCDs shown in Fig. 4.5. OTFs were prepared as discussed in Appendix B from both PSFs. The summation and subtraction of the two OTFs are shown in Fig. 4.7. As expected theoretically, the summation only contains the central sub-components and the subtraction only the axial sub-components.

Reconstruction with synthesized OTF

Two sets of dual-CCD I^5S datasets of a single bead sample were acquired. Different path length differences were intentionally introduced when acquiring these datasets. The reconstruction results using a universal OTF, taken with little path length difference present, show the expected ringing artifacts in the axial intensity profile through the bead center (Fig. 4.8(A, C)). The different polarity of the asymmetry in those plots indicates either shorter or longer path length in the movable optical path relative to the stationary one. For each dataset, we performed phase difference estimation with the method introduced in Sec. 4.2 (the results are 0.15 and -0.9 radians for dataset shown in Fig. 4.8A and C respectively), synthesized phase-adjusted OTFs with the estimate, and then reconstructed the image using the synthesized OTFs. The results are displayed again as axial intensity profiles in Fig. 4.8(B, D), which exhibit much reduced ringing compared to their counterparts in
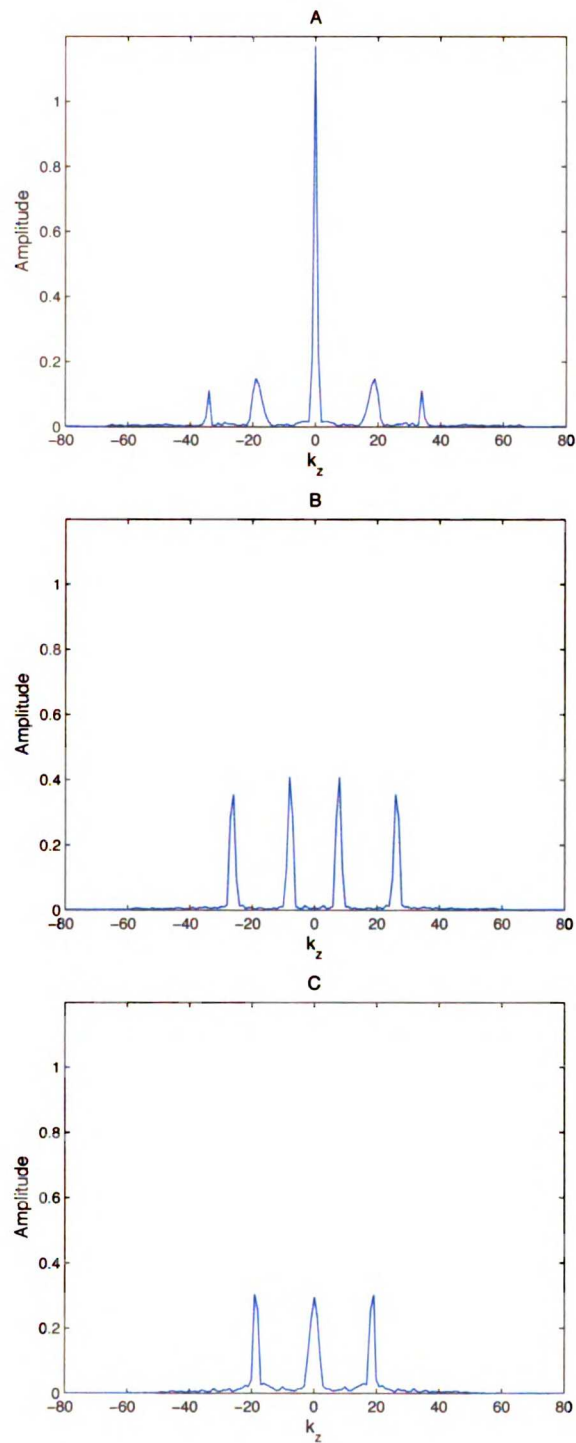
Figure 4.6: A–C are the amplitude of order 0–2 illumination structure used in I^5S, obtained by using the OTF separation method discussed in Sec. 4.3.
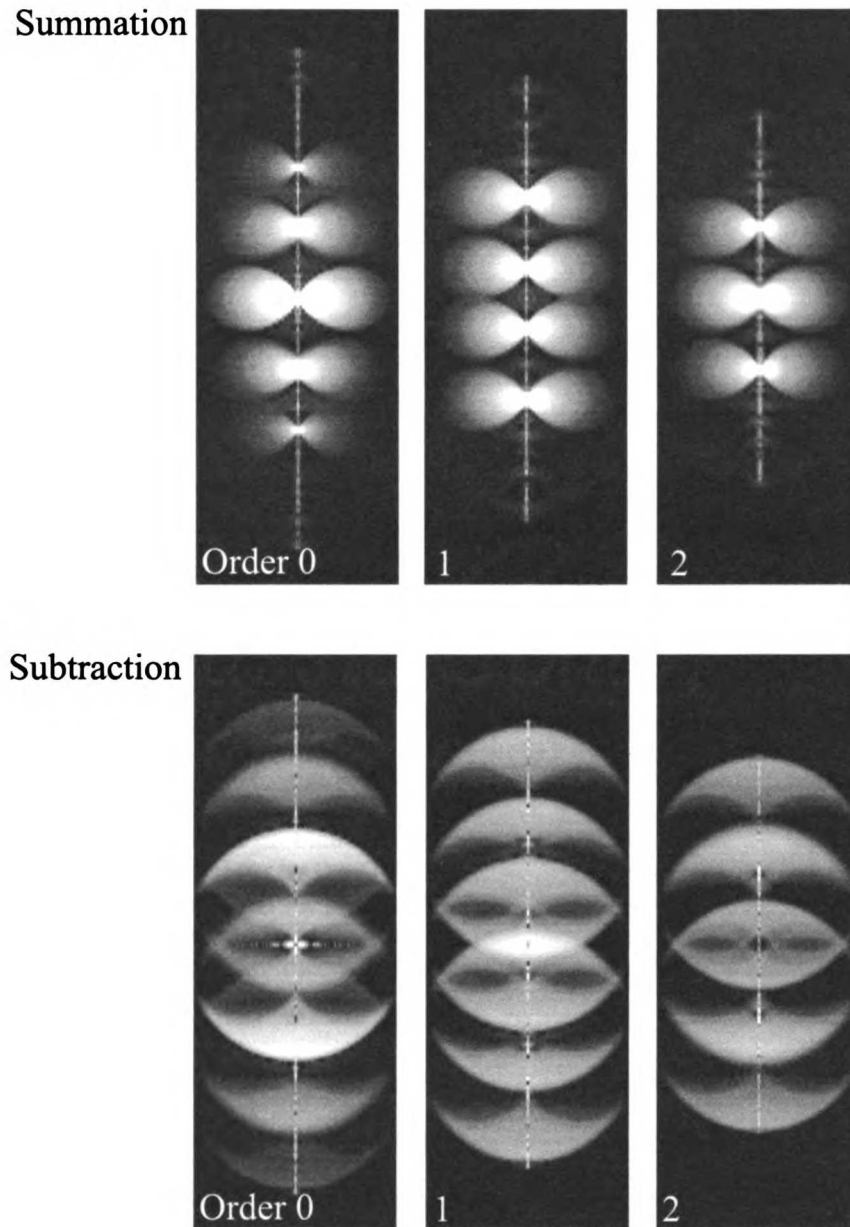
Summation

Subtraction

Figure 4.7: Summation (top panels) and subtraction (bottom panels) of the OTFs acquired from the two CCDS. As expected from the discussion in Sec. 4.2, the summation contains only the central sub-components and the subtraction only the axial (top and bottom) sub-components.
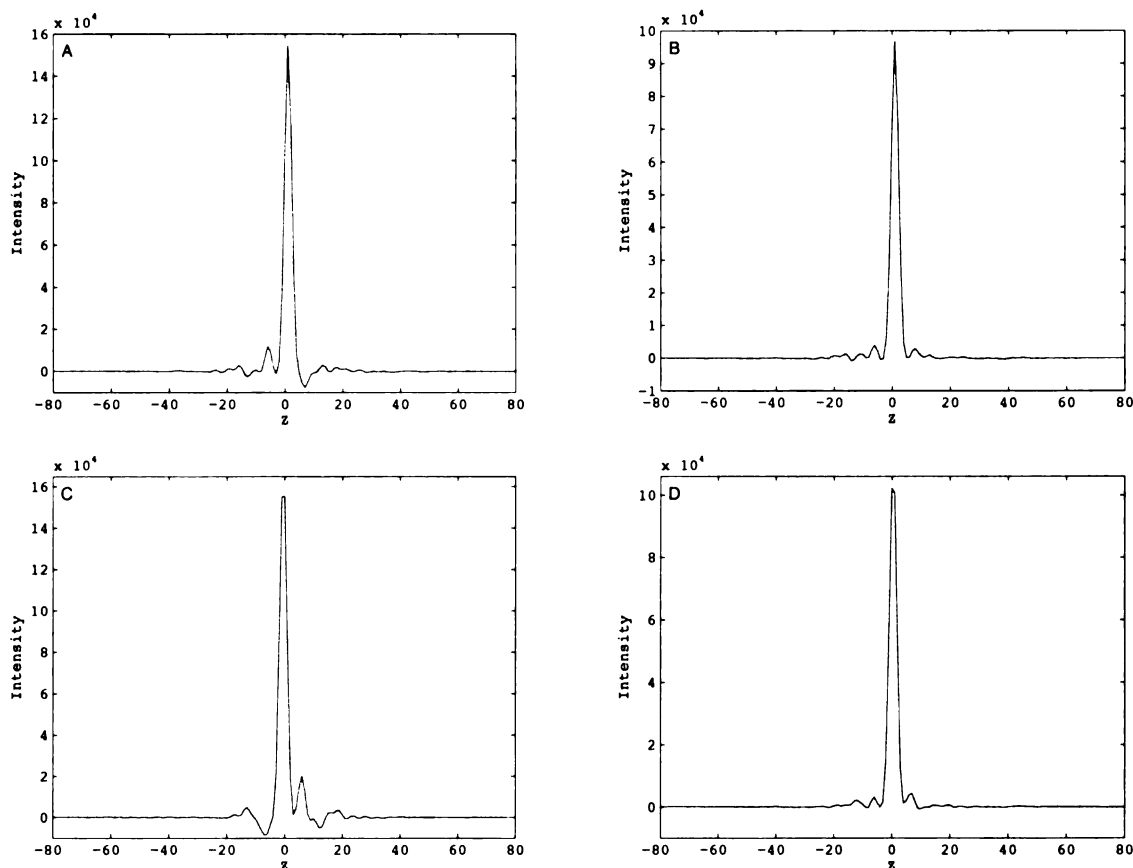
Figure 4.8: Shown in A and C are axial intensity plots through the center of a fluorescent bead reconstructed with a universal OTF from normal I^5S datasets acquired through the main beam-splitter exit. They both demonstrate the problem of ringing artifacts attributed to the phase difference inherent in the data unaccounted for by the OTF. In comparison, if the same dataset is taken through both exits of the beam-splitter, then the phase difference can be estimated (see Sec. 4.2), and phase-adjusted OTFs can be synthesized from the estimate (see Sec. 4.3) and used for reconstruction. The results thus obtained show much reduced axial ringing artifact (plotted in B and D in comparison to A and C respectively).

Fig. 4.8(A, C). This comparison clearly demonstrates the advantage of using the OTFs tailored for each dataset acquired under its unique phase difference condition, which can be estimated using the scheme developed earlier based on dual-CCD fluorescence detection.

4.5   Discussion and Outlooks

In this chapter, we have introduced the principle of how to estimate the path length difference present when acquiring each dataset with the assistance of a second CCD recording fluorescence

emission through the auxiliary exit of the beam-splitter. With the estimated phase difference, an OTF tailored for each dataset can then be synthesized based on the separability of an I^5S OTF into an I^2M OTF convolving with illumination structures, and used for reconstruction. We have used single bead experiments to prove the principle. Reconstruction using synthesized, as opposed to a universal, OTF can successfully remove most of the axial ringing artifacts that are due to the path length difference.

One major difficulty of I^5S, or any other interferometric microscope, is the strict requirement on path length equalization. This requirement must be relaxed in order to facilitate the application of I^5S to biology. The basic principle demonstrated in this chapter lays the groundwork of a scheme that can achieve such a goal.

Appendix A

Raw Data Separation

The separation of the components in Eq. 2.6 are detailed here. As suggested in Sec. 2.2.3, the easiest way of separating the terms (Tab. 2.1) making up Eq. 2.6 is to solve five such equations with five different ϕ values with the five terms as unknowns. The main disadvantage with this approach is it demands more memory space than necessary. Before explaining why this is the case we need to introduce the following facts. First of all, a complex number uses twice as much computer memory as a real number since the real and imaginary parts are both real numbers. Second, the Fourier transform of a real-number array possesses a conjugate symmetry: $\widetilde{F}(\vec{k}) = \widetilde{F}^*(-\vec{k})$, and it is hence redundant to store the full FFT array. The common practice is to just store half of the FFT array, with the other half readily obtainable when needed. Combining these two aspects, the Fourier transform of a real array therefore consumes the same amount of memory as the array before the transform. In contrast, $\widetilde{B}_{1+}$ (and likewise $\widetilde{B}_{1-}$, $\widetilde{B}_{2+}$, or $\widetilde{B}_{2-}$) has to be kept as a full FFT array since it is the Fourier transform of a complex quantity,

$$B_{m\pm}(\vec{r}) = \underbrace{(A_1 P)(\vec{r})}_{P_1} \otimes (e^{\mp i(m\vec{k}_0/2 \cdot \vec{r} + \phi_1)} D(\vec{r})), \tag{A.1}$$

as implied from Eqs. 2.3–2.5. In total, solving the five compoents of Eq. 2.6 requires a memory size of $9M$, with M being the size of the raw image data, i.e., the size of $D(\vec{r})$.

The actual separation method we used can reduce the memory size to $5M$. The loophole lies in

in Eq. A.1 which can be rewritten as

$$B_{m\pm}(\vec{r}) = \underbrace{P_m(\vec{r}) \otimes \left(\cos(m\vec{k}_0/2 \cdot \vec{r} \mp \phi_m)D(\vec{r})\right)}_{B_{mre}} \pm i \underbrace{P_m(\vec{r}) \otimes \left(\mp \sin(m\vec{k}_0/2 \cdot \vec{r} + \phi_m)D(\vec{r})\right)}_{B_{mim}}. \quad \text{(A.2)}$$

This means that all the information necessary for complex arrays B_{m+} and B_{m-} can be found in linear combination of B_{mre} and B_{mim}, four real arrays that are each M in size. Now the goal of separating the raw data has been transformed to obtaining B_0, B_{1re}, B_{1im}, B_{2re}, and B_{2im}, which occupies a combined $5M$ memory space.

The five phases of the order 1 lateral pattern were chosen to be multiples of $2\pi/5$, which become multiples of $4\pi/5$ for order 2 pattern. That is, the raw image data should, with reference to Eqs. 2.3–2.5, really be rewritten as

$$G_l(\vec{r}) = P(\vec{r}) \otimes D(\vec{r}) \quad + \quad 2P_1(\vec{r}) \otimes \left(D(\vec{r})\cos(\vec{k}_0/2 \cdot \vec{r} + \phi_0 + l \times 2\pi/5)\right)$$
$$+ \quad 2P_2(\vec{r}) \otimes \left(D(\vec{r})\cos(\vec{k}_0 \cdot \vec{r} + 2\phi_0 + l \times 4\pi/5)\right), \quad \text{(A.3)}$$

where $l = 0$ to 4 is the index of the five phases and ϕ_0 is the arbitrary reference phase first mentioned on page 16. It is easy to show that the following is true:

$$\begin{bmatrix} B_0(\vec{r}) \\ B_{1re}(\vec{r}) \\ B_{1im}(\vec{r}) \\ B_{2re}(\vec{r}) \\ B_{2im}(\vec{r}) \end{bmatrix} = \begin{bmatrix} 0.2 & 0.2 & 0.2 & 0.2 & 0.2 \\ 0.4 & 0.4\cos(2\pi/5) & 0.4\cos(4\pi/5) & 0.4\cos(6\pi/5) & 0.4\cos(8\pi/5) \\ 0.0 & 0.4\sin(2\pi/5) & 0.4\sin(4\pi/5) & 0.4\sin(6\pi/5) & 0.4\sin(8\pi/5) \\ 0.4 & 0.4\cos(4\pi/5) & 0.4\cos(8\pi/5) & 0.4\cos(12\pi/5) & 0.4\cos(16\pi/5) \\ 0.0 & 0.4\sin(4\pi/5) & 0.4\sin(8\pi/5) & 0.4\sin(12\pi/5) & 0.4\sin(16\pi/5) \end{bmatrix} \begin{bmatrix} G_0(\vec{r}) \\ G_1(\vec{r}) \\ G_2(\vec{r}) \\ G_3(\vec{r}) \\ G_4(\vec{r}) \end{bmatrix},$$

which is the approach for raw data separation in our implementation of SIM or I^5S.

Appendix B

OTF Preparation

A SIM or I^5S PSF dataset is taken using a single bead sample in the same manner as taking a normal dataset, except that only one lateral illumination pattern direction is usually sufficient. One can Fourier transform the PSF to produce the OTF, which generally displays very low signal-to-noise ratio (SNR) at high frequencies that are still within the observable region. Since the OTF is a key element in SIM/I^5S reconstruction, it would be better to have a higher SNR at high frequencies. To this end one could take advantage of the fact that an OTF in theory is radially symmetric around the optical axis. This results in the following procedure for preparing a radially averaged OTF for both SIM and I^5S.

1. Perform flat-fielding and extract the five information components (i.e., B_0, B_{1re}, B_{1im}, B_{2re}, B_{2im}) from the PSF dataset, steps involved in normal preprocessing of a dataset (see Sec. 2.2.3 and Appendix A).

2. Fourier transform each component.

3. The amplitude of the Fourier transform at every point is divided by the amplitude of a finite-sized sphere's Fourier transform at that same point (since the point source we use is not infinitesimal in size).

4. For each component, average every lateral (k_x–k_y) plane around the k_z axis in the following manner: for each pixel calculate the lateral distance from it to the k_z axis, d_l; assign the pixel

to group $\#L$ based on d_l's proximity to $L\delta$, with δ being the lateral pixel size in $1/\mu$m of the OTF; in the end the values of all pixels in each group are added up and divided by the size of each group, and a 2D radially averaged OTF is obtained.

5. For order 1 and 2, the random phase value ϕ_1 and ϕ_2 are estimated based on the following relationship: $\widetilde{B}_{1\mathrm{re}}(\vec{k}) = O_1(\widetilde{D}(\vec{k} - \vec{k}_0/2)e^{-i\phi_1} + \widetilde{D}(\vec{k} + \vec{k}_0/2)e^{i\phi_1})/2$ (from the definition of $B_{1\mathrm{re}}(\vec{r})$ in Eq. A.2). Since $\widetilde{D}(\vec{k} - \vec{k}_0/2)$ and $\widetilde{D}(\vec{k} + \vec{k}_0/2)$ are unity everywhere (for a point source), we have $\widetilde{B}_{1\mathrm{re}}(\vec{k}) = O_1(\vec{k})\cos\phi_1$, and likewise $\widetilde{B}_{1\mathrm{im}}(\vec{k}) = -O_1(\vec{k})\sin\phi_1$. Therefore, ϕ_1 can be estimated from $\widetilde{B}_{1\mathrm{re}}$ and $\widetilde{B}_{1\mathrm{im}}$ and we can obtain O_1 by $O_1(\vec{k}) = \widetilde{B}_{1\mathrm{re}}(\vec{k})\cos\phi_1 + \widetilde{B}_{1\mathrm{im}}(\vec{k})\sin(-\phi_1)$

The end product, the radially averaged OTFs of all three orders as three 2D images, is saved in one computer file for later use in reconstruction.

Appendix C

Alignment Maintenance for I⁵S

I^5S microscopy imposes strict requirements on optical alignment at multiple places of the interferometer — the movable objective lens' optic axis has to coincide with that of the stationary objective (x-, y–translation and x-, y–tilt of the movable objective); the movable objective has to focus on the same plane as the stationary objective does (z–translation of the movable objective); and the optical path length of the movable and the stationary paths have to be equal (one-dimensional translation of the movable mirror stage). The x- and y–tilt of the movable objective lens are adjusted only once when setting up the microscope. The other degrees of freedom are reduced (i.e., everything becomes aligned) prior to every experiment via using four axes of translational stage driven by piezoelectric positioning devices, as described in Sec. 3.2.2. During data acquisition, however, these stages, even under closed-loop control, can still deviate slightly from the set target mainly due to thermal drift. In addition, air flow can alter optical path length which must be compensated for by continuously resetting the movable mirror stage's target. All stages therefore have to be actively adjusted throughout the experiment, which requires accurate gauge of the stage's deviation from the initial set target.

The gauge is implemented as shown in Fig. C.1A. Two laser diode light sources, of wavelengths 670 and 780 nm, are introduced into the I^5S apparatus through two optic fibers. The 780 nm laser light is split into two halves by the beam-splitter, each of which travels to an IR reflector mounted at the back of both objectives, gets reflected, and continues traveling to the CCD where it

partially overlaps with the other half. The two diverging wavefronts generate interference fringes perpendicular to the line connecting the centers of the two wavefronts (lower-left corner in Fig. C.1B). The fringes' phase varies with, and therefore is a good indicator of, the path length difference. Periodically, such an image as Fig. C.1B is taken, the Fourier transform is performed on the subarea containing the fringes, from which the phase of the fringes can be obtained. This phase is compared to the reference phase recorded right after the initial alignment is achieved, and the difference is converted to distance by which the mirror stage has to translate back.

The 670 nm laser light passes through the two objectives and forms an image on the CCD. A specially designed wedge, installed in a filter-wheel in front of the CCD, partially reflects at this wavelength, thus bounces the beam many times and forms a series of dot images on the CCD, from which the first three are chosen to serve the alignment purpose. The middle dot is made in-focus by adjusting the axial position of the end face of the fiber transmitting the 670 nm light. The lateral position of the movable objective is monitored by the first dot's position in the image. The axial position is indicated by the peak of the parabolic curve fitted with three standard deviations of the intensity in the areas in the vicinity of the three dots (that measures how spread out the dot imgages are). Again, the deviation of these indicators of the x, y, and z position of the movable objectve from the recorded values right after initial alignment is converted into distances by which the xyz stage has to translate back.
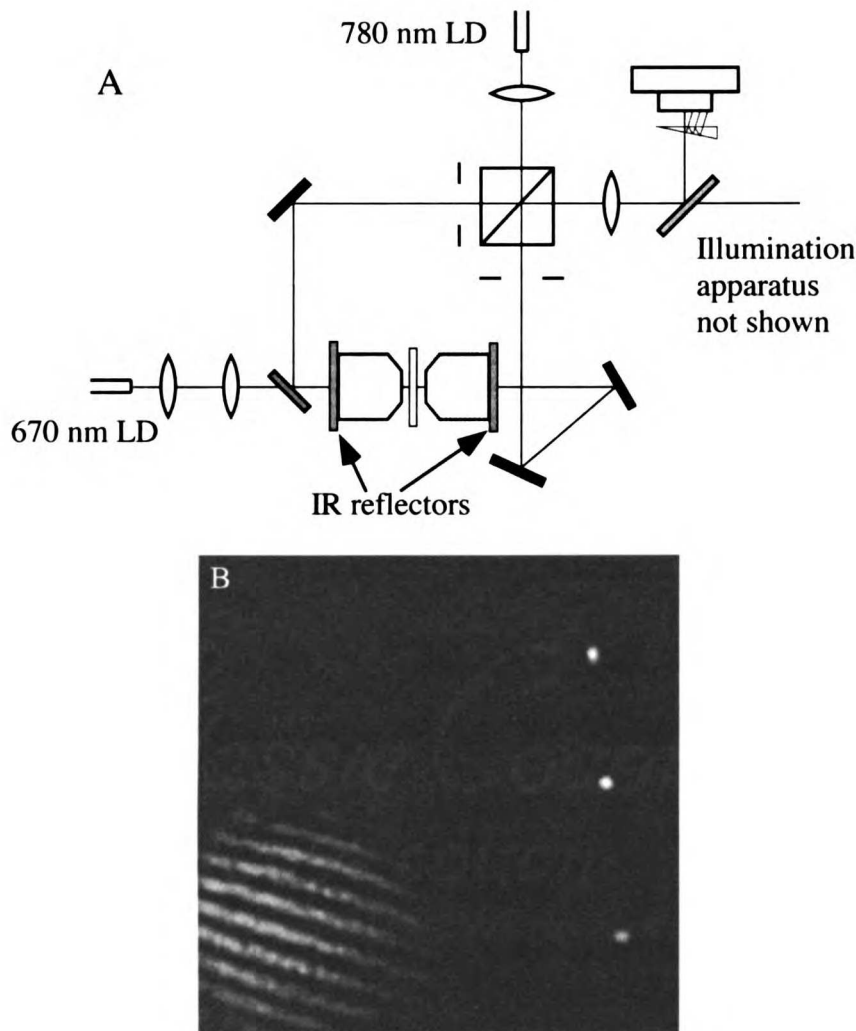
Figure C.1: Two laser diodes of wavelengths 670 and 780 nm are used in the manner shown in (A) for the maintenance of I^5S alignment during data acquisition. The 780 nm laser light is split into two halves, each travels to an IR reflector mounted at the back of both objectives, gets reflected, and continues traveling to the CCD where it partially overlaps with the other half. The two diverging wavefronts generate interference fringes perpendicular to the line connecting the centers of the two wavefronts (lower-left corner in (B)). The fringes' phase varies with, and therefore is a good indicator of, the path length difference. The 670 nm laser light passes through the two objectives and forms an image on the CCD. A specially designed wedge, installed in a filter-wheel in front of the CCD, partially reflects at this wavelength, thus bouncing the beam many times and forms a series of dot images on the CCD, from which the first three are chosen to serve the alignment purpose. The middle dot is made in-focus by adjusting the axial position of the end face of the fiber transmitting the 670 nm light. The lateral position of the movable objective is indicated by the first dot's position in the image, and the axial position by the parabolic curve fitted with three standard deviations of the intensity in the areas in the vicinity of the three dots (that measures how spread out the dot imgages are).
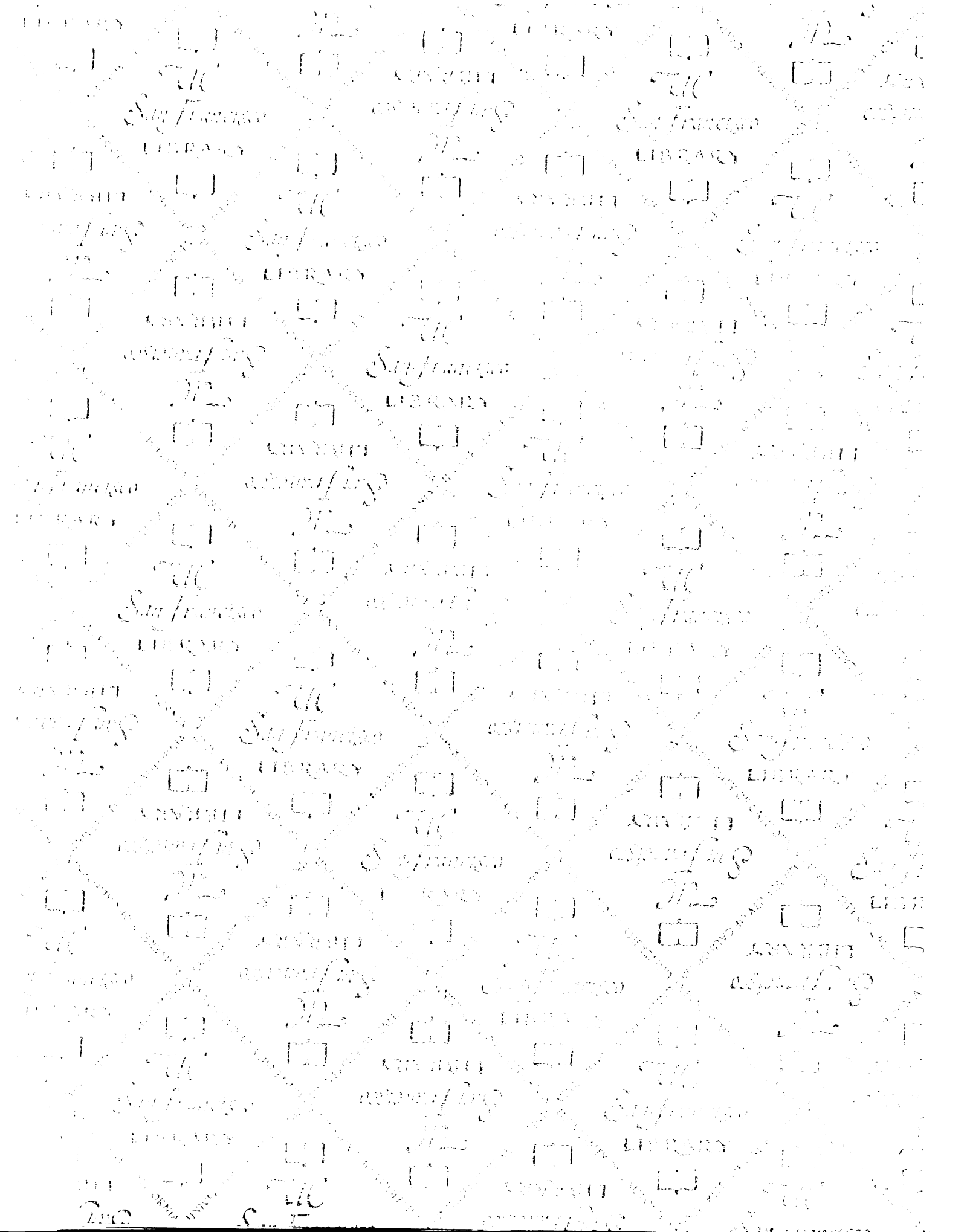
Bibliography

[1] D. A. Agard, Y. Hiraoka, P. Shaw, and J. W. Sedat. Fluorescence microscopy in three dimensions. *Methods Cell Biol.*, 30:353–377, 1989.

[2] B. Bailey, D. L. Farkas, D. L. Taylor, and F. Lanni. Enhancement of axial resolution in fluorescence microscopy by standing-wave excitation. *Nature*, 366(6450):44–48, 1993.

[3] J. E. Baldwin and C. A. Haniff. The application of interferometry to optical astronomical imaging. *Phil. Trans. R. Soc. Lond. A*, 360(1794):969–986, 2002.

[4] M. Bertero and P. Boccacci. *Introduction to Inverse Problems in Imaging*. Institute of Physics Publishing, Bristol, UK, 1998.

[5] Max Born and Emil Wolf. *Principles of Optics*. Cambridge University Press, Cambridge, UK, 6th edition, 1980.

[6] J. J. Bozzola and L. D. Russell. *Electron Microscopy*, chapter 4. Jones and Bartlett Publishers, Boston, MA, 1992.

[7] N. H. Clinthorne, T. S. Pan, P. C. Chiao, W. L. Rogers, and J. A. Stamos. Preconditioning methods for improved convergence rates in iterative reconstructions. *IEEE Trans. Medical Imaging*, 12(1):78–83, 1993.

[8] W. Denk, J. H. Strickler, and W. W. Webb. 2-photon laser scanning fluorescence microscopy. *Science*, 248(4951):73–76, 1990.

[9] A. F. Dernburg, K. McDonald, G. Moulder, R. Barstead, M. Dresser, and A. M. Villeneuve.

Meiotic recombination in c-elegans initiates by a conserved mechanism and is dispensable for homologous chromosome synapsis. *Cell*, 94(3):387–398, 1998.

[10] V. E. Foe, G. M. Odell, and B. A. Edgar. Mitosis and morphogenesis in the *Drosophila* embryo: point and counterpoint. In M. Bate and A. Martinez Arias, editors, *The development of Drosophila melanogaster*. Cold Spring Harbor Laboratory Press, Plainview, NY, 1993.

[11] J. T. Frohn, H. F. Knapp, and A. Stemmer. True optical resolution beyond the Rayleigh limit achieved by standing wave illumination. *Proc. Natl. Acad. Sci. U.S.A.*, 97(13):7232–7236, 2000.

[12] J. T. Frohn, H. F. Knapp, and A. Stemmer. Three-dimensional resolution enhancement in fluorescence microscopy by harmonic excitation. *Opt. Lett.*, 26(11):828–830, 2001.

[13] N. P. Galatsanos and A. K. Katsaggelos. Methods for choosing the regularization parameter and estimating the noise variance in image restoration and their relation. *IEEE Trans. Image Processing*, 1(3):322–336, 1992.

[14] M. Gu and C. J. R. Sheppard. Confocal fluorescent microscopy with a finite-sized circular detector. *J. Opt. Soc. Am. A*, 9(1):151–153, 1992.

[15] M. G. L. Gustafsson. Surpassing the lateral resolution limit by a factor of two using structured illumination microscopy. *J. Microsc.*, 198:82–87, 2000.

[16] M. G. L. Gustafsson, D. A. Agard, and J. W. Sedat. I^{5}M: 3D widefield light microscopy with better than 100 nm axial resolution. *J. Microsc.*, 195:10–16, 1999.

[17] M. G. L. Gustafsson, D. A. Agard, and J. W. Sedat. Doubling the lateral resolution of wide-field fluorescence microscopy using structured illumination. In *Three-Dimensional and Multidimensional Microscopy: Image Acquisition Processing VII*, volume 3919, pages 141–150, San Jose, CA, USA, 2000. SPIE.

[18] B. M. Hanser, M. G. L. Gustafsson, D. A. Agard, and J. W. Sedat. Phase retrieval for high-numerical-aperture optical systems. *Opt. Lett.*, 28(10):801–803, 2003.

[19] R. Heintzmann and C. Cremer. Laterally modulated excitation microscopy: improvement of resolution by using a diffraction grating. In *EUROPTO Conference on Optical Microscopy*, volume 3568, pages 185–196, Stockholm, Sweden, 1998. SPIE.

[20] T. Hirano, Y. Hiraoka, and M. Yanagida. A temperature-sensitive mutation of the *Schizosaccharomyces pombe* gene nuc2+ that encodes a nuclear scaffold-like protein blocks spindle elongation in mitotic anaphase. *J. Cell Biol.*, 106(4):1171–1183, 1988.

[21] Steve B. Howell. *Handbook of CCD Astronomy*, chapter 4. Cambridge University Press, Cambridge, UK, 2000.

[22] J. Huisken, J. Swoger, F. Del Bene, J. Wittbrodt, and E. H. K. Stelzer. Optical sectioning deep inside live embryos by selective plane illumination microscopy. *Science*, 305(5686):1007–1009, 2004.

[23] R. C. Jennison. A phase sensitive interferometer technique for the measurement of the fourier transforms of spatial brightness distributions of small angular extent. *Monthly Notices of the Royal Astronomical Society*, 118(3):276–284, 1958.

[24] Z. Kam, B. Hanser, M. G. L. Gustafsson, D. A. Agard, and J. W Sedat. Computational adaptive optics for live three-dimensional biological imaging. *Proc. Natl. Acad. Sci. U.S.A.*, 98(7):3790–3795, 2001.

[25] T. A. Klar, S. Jakobs, M. Dyba, A. Egner, and S. W. Hell. Fluorescence microscopy with diffraction resolution barrier broken by stimulated emission. *Proc. Natl. Acad. Sci. U.S.A.*, 97(15):8206–8210, 2000.

[26] M. G. Lowenstein, T. D. Goddard, and J. W. Sedat. Long-range interphase chromosome organization in Drosophila: a study using color barcoded fluorescence in situ hybridization and structural clustering analysis. *Mol. Biol. Cell*, 15(12):5678–5692, 2004.

[27] C. W. McCutchen. Two families of apodization problems. *J. Opt. Soc. Am.*, 59(9):1163–1171, 1969.

[28] M. Minsky. Microscopy apparatus. *US patent 3,013,467,* Dec. 19, 1961.

[29] M. A. A. Neil, A. Squire, R. Juškaitis, P. I. H. Bastiaens, and T. Wilson. Wide-field optically sectioning fluorescence microscopy with laser illumination. *J. Microsc.,* 197:1–4, 2000.

[30] A. Papoulis. Apodization for optimum imaging of smooth objects. *J. Opt. Soc. Am.,* 62(12):1423–1429, 1972.

[31] I. Reim, R. Stanewsky, and H. Saumweber. The puff-specific RRM protein NonA is a single-stranded nucleic acid binding protein. *Chromosoma,* 108:162–172, 1999.

[32] D. L. Riddle, T. Blumenthal, B. J. Meyer, and J. R. Priess, editors. *C. elegans II.* Cold Spring Harbor Laboratory Press, Plainview, N.Y., 1997.

[33] M. Ryle and A. Hewish. The synthesis of large radio telescopes. *Monthly Notices of the Royal Astronomical Society,* 120(3):220–230, 1960.

[34] M. Schrader, K. Bahlmann, G. Giese, and S. W. Hell. 4pi-confocal imaging in fixed biological specimens. *Biophy. J.,* 75(4):1659–1668, 1998.

[35] G. Servant, O. D. Weiner, P. Herzmark, T. Balla, J. W. Sedat, and H. R. Bourne. Polarization of chemoattractant receptor signaling during neutrophil chemotaxis. *Science,* 287(5455):1037–1040, 2000.

[36] P. Török, P. Varga, Z. Laczik, and G. R. Booker. Electromagnetic diffraction of light focused through a planar interface between materials of mismatched refractive indices: an integral representation. *J. Opt. Soc. Am. A,* 12(2):325–332, 1995.

[37] P. J. Verveer and T. M. Jovin. Efficient superresolution restoration algorithms using maximum a posteriori estimations with application to fluorescence microscopy. *J. Opt. Soc. Am. A,* 14(8):1696–1706, 1997.

[38] T. Wilson. The role of the pinhole in confocal imaging system. In J. B. Pawley, editor, *Handbook of Biological Confocal Microscopy.* Plenum Press, New York, 1995.